Synthesis of Highly Porous Mn_2O_3-Doped Fe_3O_4 NPs with a Dual Catalytic Function Using Asymmetric Water Soluble Mn-Salen Complex as a Reducing Agent and Template: Catalytic Activity over One-Pot Strecker Synthesis from Alcohols in Recyclable TAIm[CN] Ionic Liquid

Eman Khalaf[1] · Ameer A. Alameri[2] · Jitendra Malviya[3] · T. CH. Anil Kumar[4] · Farag M. A. Altalbawy[5,6] · Raed H. C. Alfilh[7] · Milad Kazemnejadi[8]

Abstract

An asymmetric Mn/TEMPO-Salen complex was utilized as a reducing agent and template for the synthesis of Mn/TEMPO-doped Fe_3O_4 NPs in situ. The subsequent thermal decomposition of Mn/TEMPO-doped Fe_3O_4 NPs, as a precursor, provides the highly porous ($641 \ m^2 \ g^{-1}$) Mn_2O_3-doped Fe_3O_4 NPs. The highly porous NPs was characterized by FTIR, BET, TGA, VSM, ICP, TEM, XRD, UV–Vis, and XPS analyses. High stability and catalytic activity was found for the NPs in the synthesis of α-aminonitriles via the Strecker synthesis from primary and secondary alcohols under mild conditions. TAIm[CN] ionic liquid (IL) was used as an efficient solvent and nitrile-required reagent to synthesis of α-aminonitriles. TAIm[CN] IL could be recycled for several times by a simple recovery and subsequent treatment. Also, the catalytic activity of the NPs was evaluated toward the selective alcohol oxidation to carbonyl compounds and the direct transformation of imines from alcohols and aryl amines. Mn_2O_3-doped Fe_3O_4 NPs could be recovered and reused for several consecutive cycles without any considerable reactivity loss.

Graphical Abstract

Highly porous MnO-doped Fe_3O_4 NPs were synthesized via thermal decomposition of Mn/TEMPO-doped Fe_3O_4 NPs as a precursor, and used as an efficient recyclable catalyst for the Strecker synthesis from alcohols in TAIm[CN] ionic liquid
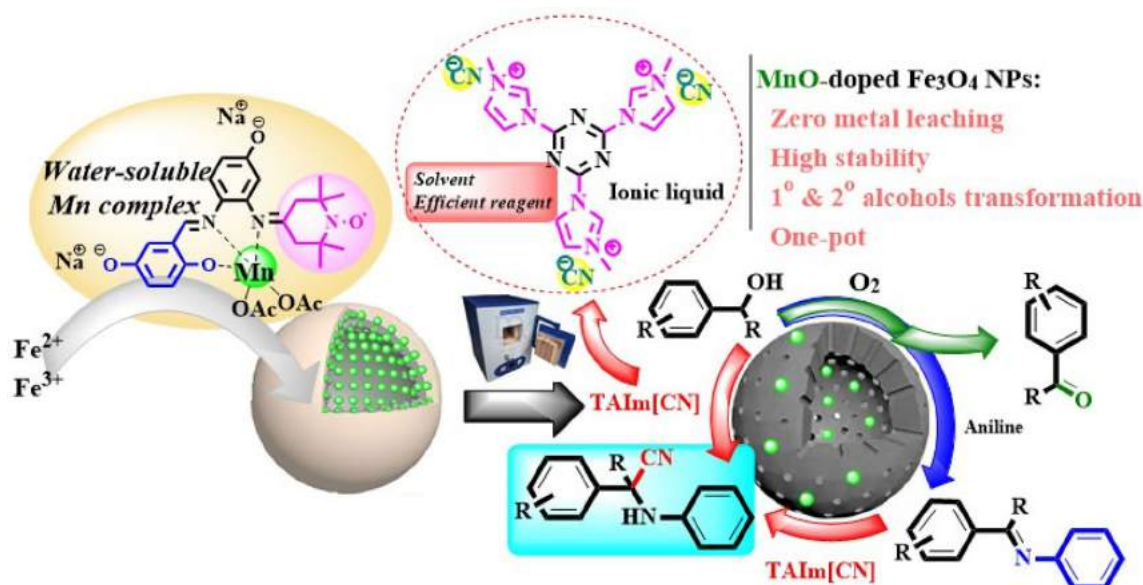
Extended author information available on the last page of the article

Springer

1 Introduction

Strecker synthesis is one of the multicomponent reactions for the effective preparation of α-aminonitriles and α-amino acids [1, 2]. Despite the fact that the Strecker synthesis was discovered centuries ago, it is a reliable, cheap, and accessible three-component reaction for the one-pot preparation of α-aminonitriles from aldehyde, amine, and a nitrile source (hydrogen cyanide or alkali cyanide salt), both on a laboratory scale and an industrial scale [2]. α-Aminonitriles are valuable building blocks for the preparation of bioactive compounds such as heterocyclic nitrogen-containing compounds (such as imidazole and thiadiazole), 1,2-diamines, amides, and α-amino-aldehydes, α-amino alcohols, α-amino acids, etc [1, 2].

Application of Strecker reaction in the synthesis of pharmaceutical compounds such as benzofuran derivatives [3], saframycin A [4], saxagliptin [5], (±)-phthalascidin 622 [6], ecteinascidin 743 [7], and hepatitis C virus NS3 serine protease inhibitors [8] is well known. However, the hash applied reaction conditions, the use of toxic and non-recyclable nitrile reagents (like TMSCN), and the incompatibility with different substrates have led to the development of different catalytic systems for the Strecker synthesis. Various catalytic systems have been reported for this reaction, including organocatalysts, polymeric materials and resins, homogenous Lewis acids, heterogeneous Brønsted acids, heterogeneous Lewis acids, ionic liquids, metal complexes, and metal NPs [9].

Porous NPs due to their unique catalytic properties, very high surface to volume ratio, and high pore volume have attracted a lot of attention in organic synthesis as effective catalysts [10]. High porosity in this NPs due to the presence of active catalytic centers and also providing effective concentration in these pores, causes the reactions to be effectively catalyzed.

Eslami et al. introduced MCM-41 mesoporous silica as an efficient catalyst for the synthesis of α-aminonitriles [10]. Recently, the Strecker synthesis of α-aminonitriles was performed using Au NPs capped with porous silica shell [11]. Sulfonated nanoporous carbon catalyst (CMK-5-SO$_3$H) [12], mesoporous indium metal–organic framework (MOF) [13], and Pd supported on methane diamine (propyl silane) functionalized Fe_3O_4 NPs [14], were some the catalysts-based porous nanomaterials in the Strecker synthesis.

Due to the ease of separation and easy work-up, magnetic NPs have been used as a core in many catalytic systems;

However, magnetic NPs alone lack significant catalytic properties in organic synthesis [1]. Magnetic Fe_3O_4 NPs are covered with silicate groups due to their high tendency to agglomerate and also in order to be functionalized with other groups required for a desired reaction. These processes are not only uneconomical, but multiple steps to prepare a catalyst are exhausting and each step suffers some loss of efficiency.

Synthesis of metal-doped magnetite NPs is one of the strategies that eliminates the need for successive functionalizations in order to prepare nanoparticles with unique catalytic activity [15, 16]. The results have shown that doped transition metal-nanocatalysts increase the catalytic properties compared to the same non-doped sample [17]. Recently, Kaur et al. demonstrated this enhancement in catalytic activity of Mn^{2+}-doped supported Pd nano-catalysts in comparison with undoped counterparts for reduction, oxidation, and C–C coupling [18]. In another report, enhances H_2O_2 oxidation of carbamazepine was catalyzed by Cu(I)-doped Fe_3O_4 NPs/porous C composite with higher specific TOF and oxidation efficiency than Fe_3O_4 and $Fe_{2.85}Cu_{0.15}O_4$ [18]. Doping of transition metals in magnetite NPs structures is done by various methods, which can be mentioned as electrosynthesis [19] and electrodeposition [20] as the most common ones.

One of the affordable and reliable ways to prepare metal oxide NPs is the thermal decomposition of Schiff base complexes of transition metals [21–23]. For example, Rezazadeh et al. prepared CuO, NiO, and Co_2O_3 metal oxide NPs from polysalicylaldehyde-metal Schiff base complexes as a precursor [21]. According to the literature reports, by removing the organic template, metal oxide NPs can be prepared. Other metal-oxide NPs have also been reported for the preparation of γ-Fe_2O_3 and Co_3O_4 [22], and mesoporous-MgO/expanded graphite [23] by the respective organic templates. However, if this thermal decomposition and the preparation process of metal oxide NPs takes place in a larger framework (mother), the thermal decomposition of the organic template leads to a very porous structure [24]. The requirement of this process is the preparation of the mother NPs by a reagent (a reducing agent for metal ions) that is placed in the mother structure as a template, so that after thermal decomposition and removal of the template, they were doped as a metal oxide in the mother structure.

Traditionally, the preparation of metal nanoparticles is done in the presence of a reducing agent. Aqueous extracts of different parts of plants, which are rich in phenolic
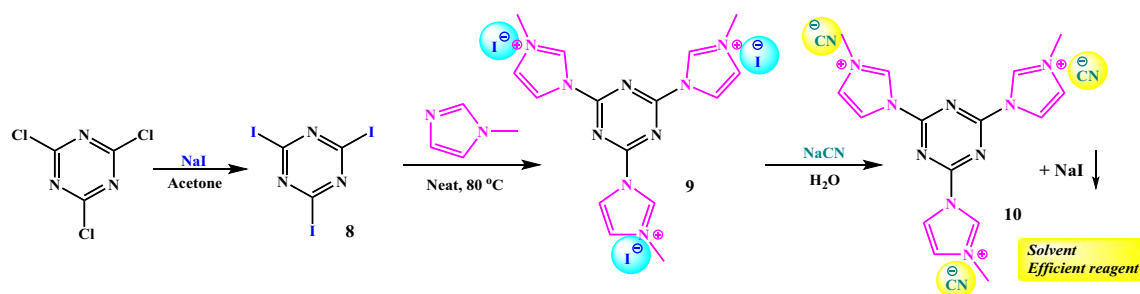
Scheme 1 Synthesis of TAIm[CN] ionic liquid from TAIm[I] ionic liquid [31–34]

compounds, are known as powerful reducing agents. However, the failure to obtain a single formulation, the failure to obtain a single percentage composition for a plant extract, and the failure to obtain the type of extract used by researchers in different parts of the world, severely limits the reproducibility of the method. Therefore, the use of synthetic reducing agents not only solves the mentioned limitations, but also, by designing a unique reducing agent, the morphology and catalytic properties of the resulting nanoparticle can be modified.

In addition to extracts of various plant organs, α-D-Glucose [25], citric acid [26], sodium citrate [27], ethylene glycol [28], and NaOH [29], also been used as reducing agents to prepare Fe₃O₄ NPs. Also, TEMPO has been used as an auxiliary and reducing agent in the preparation of CoO NPs [30]. Therefore, the synthesis of a phenolic compound with TEMPO groups suggests that it is an effective reductant for metal ions and the formation of nanostructures.

Another limitation of Strecker synthesis is the use of toxic, expensive and non-recyclable reagents such as TMSCN, which not only limits its application on an industrial scale, but also brings environmental problems. Modified ionic liquids are a smart strategy for the benefit of the environment, so that in addition to using them as a solvent, they can also be used as an effective reagent by modifying their counter anion. The TAIm[I] ionic liquid (Based on the 1, 3, 5-Triazine Framework) is one of the known ionic liquids that has the ability to exchange counter anion with different types of other anions. With the exchange of [I] by [OH], the resulting TAIm[OH] ionic liquid was used as a solvent and a basic reagent for the transesterification, aldol condensation [31] and coupling reactions [32]. Also, TAIm[N₃] ionic liquid (anion exchange of [I] with [N₃] in TAIm[I]) was used as an effective solvent and reagent for the preparation of tetrazole derivatives [33]. In a recent study, it was also shown that replacing iodide with the oxidizing salts such as MnO₄²⁻, provides TAIm[MnO₄] IL as an efficient solvent and reagent for the selective oxidation of alcohols [34]. The results suggest that the preparation of TAIm[CN] IL through anion exchange of [I] with [CN] (in the presence of NaCN

salt), makes it an effective alternative to toxic, expensive and unstable reagents such as TMSCN, that was studied in this work. The liquidity of these ionic liquids at room temperature as well as their high boiling point has made it possible to use them not only as a solvent at high temperatures, but by modifying them, they can also be used as an effective reagent in organic synthesis (Scheme 1). The recyclability of these ionic liquids without loss of activity makes the process cost-effective and sustains the environment.

In this work, Mn₂O₃ NPs were prepared in situ within the framework of Fe₃O₄ and created a highly porous structure due to the thermal decomposition of the Mn/TEMPO Salen complex within Fe₃O₄ (Scheme 2). The water-soluble sodium salt of the Mn/TEMPO Salen complex acts as a capping agent and reduces Fe^{3+} and Fe^{2+} ions and forms Mn/TEMPO-doped Fe₃O₄ NPs. Thermal decomposition of these NPs produced highly porous Mn₂O₃-doped Fe₃O₄ NPs with unique catalytic properties for the direct preparation of α-aminonitriles from alcohols. Mn₂O₃-doped Fe₃O₄ NPs in the presence of molecular oxygen cause the selective oxidation of alcohols to the corresponding carbonyl, which in the presence of amine and TAIm[CN] IL gives the corresponding α-aminonitrile product. TAIm [CN] was used as an effective solvent and recyclable reagent in this transformation (Scheme 1).

2 Experimental

2.1 Materials and Instrumentation

All materials were provided from Merck and Fluka companies and used as received without any further purification. All used solvents were dried before use. GC analyses were conducted on an Agilent GC7890-MS5975 (USA) instrument with a CBP5 column (Shimadzu 30 m 9 0.32 mm 9 0.25 mm). Fourier transform infrared (FTIR) spectra were taken on a JASCO instrument model V-570. ¹HNMR (400 MHz) and ¹³CNMR (100 MHz) spectra were recorded using a Bruker Ascend NMR 400 MHz
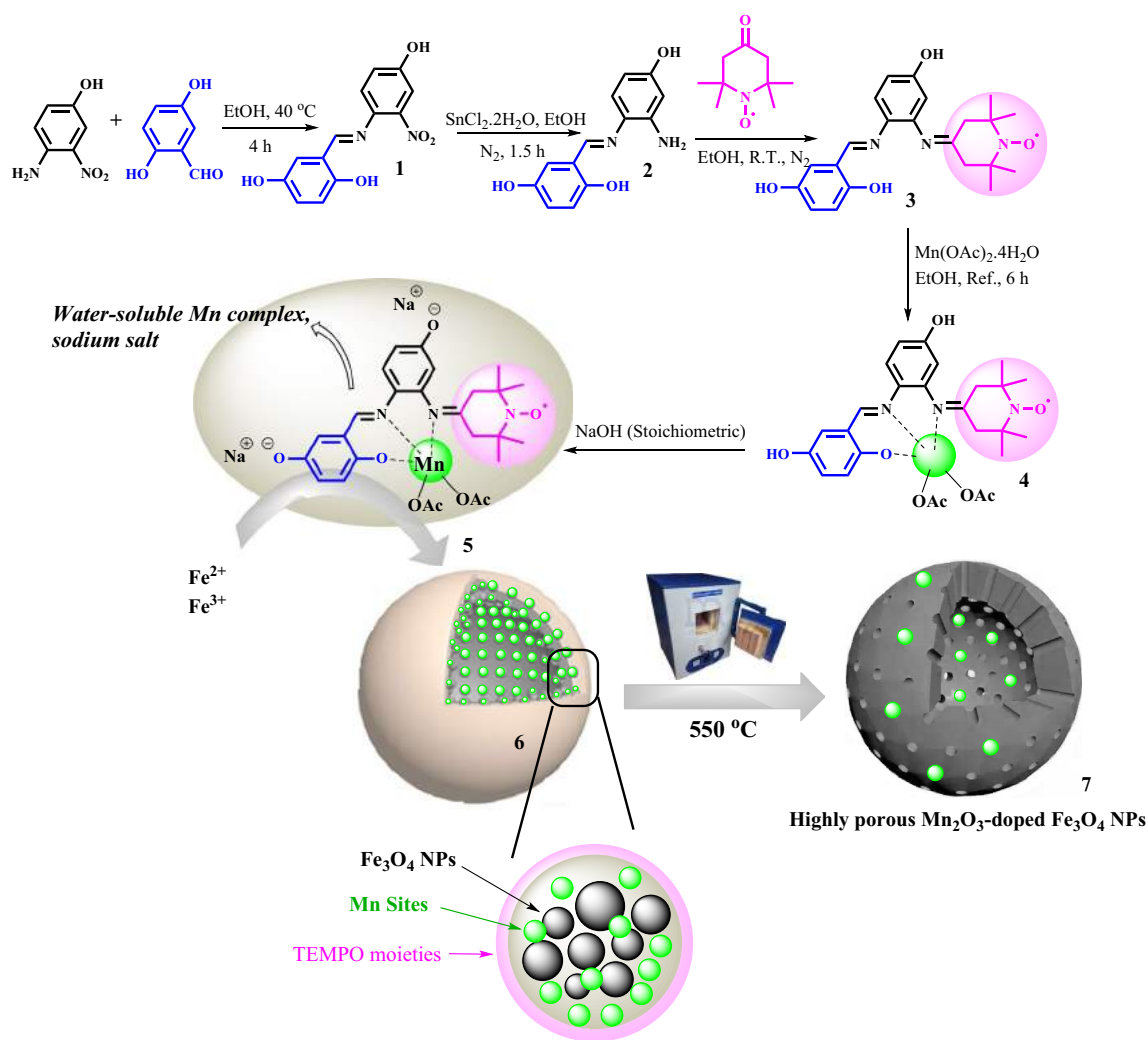
Scheme 2 A general schematic view for the synthesis of Mn_2O_3-doped Fe_3O_4 NPs from the thermal decomposition of Mn/TEMPO-doped Fe_3O_4 NPs

in ultra-pure deuterated solvents. TMS was used as an internal standard for the NMR analyses. XPS analysis was conducted on a XR3E2 (VG Microtech) twin anode X-ray source with radiation of Al-Kα = 1486.6 eV. TEM images were taken using a Philips EM208 microscope, operated at 100 kV. Dynamic light scattering (DLS) and zeta potentials of the samples were obtained using a zeta potential analyzer from Malvern Instruments Ltd. The viscosity of the ILs was measured by a Thermo Scientific™ HAAKE™ Viscotester™ apparatus at ambient temperature. Thermogravimetric analyses (TGA) of the NPs were performed on a NETZSCH STA 409 PC/PG under air atmosphere with a heating rate of 10 °C min^{-1} in a temperature range of 25–850 °C. Lake Shore vibrating sample magnetometer (VSM) was served for studying the magnetic properties of the NPs. Inductively coupled plasma—optical emission spectrometry (ICP-OES)

analysis was perfumed on a VARIAN VISTA-PRO CCD simultaneous ICP-OES instrument to determine metal leaching and Mn contents of the NPs. Also, ICP-MS analyses were performed on a ELAN 6100 DRC-e, Perkin Elmer instrument. Energy dispersive X-ray spectroscopy (EDX) analyses were accomplished on a field emission scanning electron microscope, FE-SEM, JEOL 7600F, equipped with an energy dispersive X-ray spectrometer from Oxford Instruments. Crystal structure of the NPs were performed using a Bruker D8/Advance powder X-ray diffractometer, and using a HAAKE D8 recirculating bath, the cell temperature was maintained at 25.0 °C. Elemental analyses of the Schiff base compounds (**1**–**4**) were conducted on a CHN ThermoFinnigan Flash EA 1112 instrument. The specific surface area, pore diameter, and pore volume of the obtained NPs were studied by N_2 physisorption at −196 °C on a Micromeritics ASAP 2000 instrument using

the BET method. Ultraviolet–visible (UV–Vis) spectra were recorded on a SPECORD 210 PLUS Analytikjena spectrophotometer.

2.2 Synthesis of 2-[((4-Hydroxy-2-nitrophenyl) imino)methyl]benzene-1,4-diol (1)

2-(((4-Hydroxy-2-nitrophenyl)imino)methyl)benzene-1,4-diol (Schiff base **1**) was simply prepared by condensation of 4-amino-3-nitrophenol (2.0 mmol) and 2,5-dihydroxybenzaldehyde (2.5 mmol) in absolute EtOH (20 mL) at 40 °C for 4 h. The resulting yellow precipitate was filtered and purified by recrystallization in hot EtOH (98% isolated yield).

*Characterization data for **1**: m.p. 307–310 °C; ^{1}H-NMR (400 MHz, CDCl$_3$) δ(ppm): 6.6 (d, J = 7.5 Hz, 1H), 6.8 (d, J = 7.5 Hz, 1H), 6.9 (s, 1H), 7.1 (d, J = 8.0 Hz, 1H), 7.3 (d, J = 8.0 Hz, 1H), 7.5 (s, 1H), 8.5 (s, 1H), 9.0 (s, 1H), 9.4 (s, 1H), 12.6 (s, 1H); ^{13}C-NMR (100 MHz, CDCl$_3$) δ(ppm): 110.4, 118.1, 118.6, 119.2, 121.9, 122.4, 127.1, 134.3, 142.8, 148.8, 156.0, 158.1, 163.0; CHN analysis for C$_{13}$H$_{10}$N$_2$O$_2$: Found %: C 56.90; H 3.70, N 10.24. Calculated, %: C 56.94; H 3.68, N 10.22.*

2.3 Synthesis of 2-[((2-Amino-4-hydroxyphenyl) imino)methyl]benzene-1,4-diol (2) by the Selective Reduction of Nitro Group

Selective reduction of nitro group in Schiff base **1** (1.0 mmol) to 2-[((2-amino-4-hydroxyphenyl)imino) methyl]benzene-1,4-diol (Schiff base **2**) was performed according to a previously reported protocol using SnCl$_2$·2H$_2$O (5.0 mmol) in 5.0 mL of absolute EtOH [35]. The reaction was refluxed under N$_2$ atmosphere for the appropriate time monitored by TLC. Upon reaction complexion (95 min), the mixture was allowed to cool down, then the mixture was poured into ice. The pH of the solution was adjusted to 7.0 by aqueous NaHCO$_3$ 5%. Then, the product was extracted to EtOAc twice, and the resulting organic phase was dried over MgSO$_4$. Schiff base **2** (94% isolated yield) was dried in oven and stored as a pale yellow powder.

*Characterization data for **2**: m.p. 317–320 °C; ^{1}H-NMR (400 MHz, CDCl$_3$) δ(ppm): 5.2 (s, 2H), 6.1 (s, 1H), 6.4 (d, J = 8.0, 1H), 6.6 (d, J = 8.0, 1H), 6.7 (s, 1H), 6.7 (d, J = 8.0, 1H), 6.9 (d, J = 8.0, 1H), 8.0 (s, 1H), 8.3 (s, 1H), 9.4 (s, 1H), 12.7 (s, 1H); ^{13}C-NMR (100 MHz, CDCl$_3$) δ(ppm): 102.4, 109.5, 118.1, 118.6, 119.6, 121.9, 125.4, 125.5, 144.4, 148.8, 156.2, 157.9, 161.7; CHN analysis for C$_{13}$H$_{12}$N$_2$O$_3$: Found %: C 63.96; H 4.93, N 11.46. Calculated, %: C 63.93; H 4.95, N 11.47.*

2.4 Synthesis of Asymmetric Ligand (3) and Its Mn Complex (4)

In following, the asymmetric ligand (**3**) was synthesized by dissolution of 2.0 mmol 4-oxo-2,2,6,6-tetramethylpiperidine 1-oxyl (4-oxo-TEMPO) and Schiff base **2** (2.0 mmol) in 10 mL of EtOH at room temperature. The reaction was stirred at room temperature for 8 h under N$_2$ atmosphere. The resulting orange sediments were filtered, washed with cool EtOH and recrystallized into hot EtOH for more purification. The resulting asymmetric ligand (**3**) was used as a reducing agent for the synthesis of magnetite NPs.

To NMR analysis of asymmetric ligand **3**, it was treated with sodium ascorbate to reduce TEMPO moieties to TEMPOH, according to a previously reported protocol [36]. Briefly, asymmetric ligand **3** (0.5 mmol) was dispersed in an aqueous solution of sodium ascorbate (0.8 mmol in 1.5 mL distilled water). The mixture was shaken for 1 h. The product was then extracted to CHCl$_3$, dried over Na$_2$CO$_3$, and finally dried in vacuum oven for 24 h (50 °C).

*Characterization data for **3**: m.p. 235–240 °C; ^{1}H-NMR (400 MHz, CDCl$_3$) δ(ppm):1.25 (s, 12H), 2.29 (s, 4H), 6.66–7.20 (m, 6H, Ar–H), 7.81 (s, 1H), 8.48 (s, 1H), 9.27 (s, 1H), 12.74 (s, 1H); ^{13}C-NMR (100 MHz, CDCl$_3$) δ(ppm): 28.2, 41.9, 42.7, 59.8, 111.8, 117.8, 118.1, 118.4, 122.6, 126.8, 136.5, 144.7, 148.7, 156.0, 160.8, 163.6, 188.9; Found %: C 66.65; H 6.58, N 10.24. Calculated, %: C 66.65; H 6.61, N 10.27.*

To coordinate Mn ions to the asymmetric ligand (**3**), Mn(OAc)$_2$·4H$_2$O (1.0 mmol) and the asymmetric ligand (**3**) was dissolved in 20 mL of EtOH. The mixture was stirred for 6 h under reflux conditions. The resulting brown sediments were filtered, washed with deionized water, dried and stored at room temperature.

2.5 Synthesis of Mn/TEMPO-Doped Fe$_3$O$_4$ NPs Using the Asymmetric Mn-Salen Complex (4) as a Reducing Agent

A traditional procedure was applied for the synthesis of Mn/TEMPO-doped Fe$_3$O$_4$ NPs [1, 37] in the presence of the asymmetric Mn-salen complex (**4**) as a reducing agent. FeCl$_3$·H$_2$O (1.3 g) and FeCl$_2$·4$_2$O (0.9 g) was added to the 800 mL of distilled water. The reaction temperature and pH of the solutions were adjusted to 80 °C and 9.0 (using NaOH 0.1 N) respectively. Then, an aqueous solution of asymmetric Mn-salen complex (**4**) (1.0 g) in stoichiometric NaOH (1.6 g, 2.0 mmol) in 25 mL of deionized water was added dropwise to the solution under open air conditions. The addition was continued (10.0 mL) until the solution turn to black completely. Then, the mixture was refluxed for 4 h and the resulting Mn/TEMPO-doped Fe$_3$O$_4$ NPs was

collected/separated by an external magnetic field, washed with deionized water and EtOH respectively, and dried into a vacuum oven.

2.6 Synthesis of Mn$_2$O$_3$-Doped Fe$_3$O$_4$ NPs via Thermal Decomposition of Mn/TEMPO-Doped Fe$_3$O$_4$ NPs

Mn$_2$O$_3$-doped Fe$_3$O$_4$ NPs was simply synthesized by the thermal decomposition of Mn/TEMPO-doped Fe$_3$O$_4$ NPs, as a template. Mn$_2$O$_3$-doped Fe$_3$O$_4$ NPs (200 mg) was calcinated at 550 °C for 3 h under air atmosphere to remove the organic groups (TEMPO-Salen moieties). Then, the resulting NPs was washed with deionized water and further by absolute MeOH, and dried and stored at ambient temperature.

2.7 Synthesis of TAIm[I] and TAIm[CN] Ionic Liquids

TAIm[I] IL was synthesized and characterized by the previously reported procedures [31–34]. Then, to synthesis of TAIm[CN] IL, 7.0 mmol of NaCN salt was added to the mixture of TAIm[I] IL (2.0 mL, 6.5 mmol) in 2.0 mL of distilled water at room temperature, and the mixture was stirred for 4 h. Then, the mixture was filtered and the resulting ionic liquid product (TAIm[CN] IL) was extracted to *n*-BuOH (3×5) from the residue. Finally, the solvent (*n*-BuOH) was removed under reduced pressure and the product was isolated in refrigerator at 4 °C.

2.8 General Procedure for Mn$_2$O$_3$-Doped Fe$_3$O$_4$ NPs-Catalyzed Synthesis of α-Aminonitriles from Alcohols

2.8.1 For Primary Alcohols

A Schlenk flask equipped with a O$_2$ bubbling syringe was charged with TAIm[CN] IL (2.0 mL), Mn$_2$O$_3$-doped Fe$_3$O$_4$ NPs (2.0 mg, 0.4 mol Mn), alcohol (1.2 mmol), amine (1.0 mmol), and a stirrer bar. The reaction was stirred at room temperature with 15 mL min^{-1} O$_2$ bubbling flow rate volume. The reaction progress was monitored by TLC analysis at various time intervals. Upon the reaction completion, the magnetic NPs was separated by an external magnetic field, washed with EtOH and DEE, and reused for the next run after drying. Then, 2.0 mL distilled water and 2.0 mL of CHCl$_3$ was added to the residue. The aqueous layer containing TAIm[CN] IL was separated and treated with 2.0 mL NaCN for 1.0 h. TAIm[CN] IL was recovered after removal of water under reduced pressure. The desired α-aminonitrile was separated from the organic phase after removal of solvent under reduced pressure and drying over Na$_2$SO$_4$. The resulting crude product was purified by recrystallization

in EtOH. The products were characterized by ^{1}HNMR, ^{13}CNMR, and melting points and comparison with the authentic reports.

2.8.2 For Secondary Alcohols

The direct transformation of secondary alcohols was performed under 20 mL min^{-1} O$_2$ flow rate volume at 80 °C.

2.9 Surface Acidity Measurement of Mn$_2$O$_3$-Doped Fe$_3$O$_4$ NPs by the Pyridine Adsorption Assay

The Lewis acid character of Mn$_2$O$_3$-doped Fe$_3$O$_4$ NPs surface was investigated qualitatively by the pyridine surface absorption test according to the procedure provided by Nasseri et al. [62]. Briefly, identical tablets prepared from the NPs with a ratio of 1:10 in the presence of KBr treated with different concentrations of pyridine including 0.005, 0.01, and 0.1 M of pyridine. Then, the tablets treated with pyridine were degassed at 150 °C for 1 h. FTIR analysis of the resulting tablets were recorded in the range of 400–4000 cm^{-1}.

3 Results and Discussion

3.1 Characterization of NPs

Compounds **1**–**5** were successfully characterized by elemental (CHN) analysis (experimental section), FTIR (Fig. S1), ^{1}HNMR (Figs. S2,S4,S6) and ^{13}CNMR (Figs. S3,S5,S7) analyses. Next, the physical properties of TAIm[CN] and TAIm[I] ILs were studied. Table 1 shows some of these properties including density, viscosity, appearance, and molecular weight. In accordance with the previous reports, the density and viscosity for TAIm[I] IL were measured to be 1.84 g cm^{-3} and 1182 cP, respectively [31–34]. Also, for TAIm[CN] IL, the density and viscosity were determined as 1.42 g cm^{-3} and 1190 cP, respectively.

Figure 1 shows the EDX analysis for TAIm[CN] and TAIm[I] ILs. The presence of peaks related to the iodide binding energy in 3.9, 4.1, 4.5, and 4.9 eV and also the absence of Cl in the EDX spectrum of the TAIm[I] IL

Table 1 Physical properties of TAIm[I] [31–34] and TAIm[CN] ILs

Ionic liquid	Mw (g mol^{-1})	Physical properties		
		Color/appearance	Density (g cm^{-3})	Viscosity (cP)
TAIm[I]	705.0	Dark yellow oil	1.84	1182
TAIm[CN]	402.4	Pale yellow oil	1.42	1190
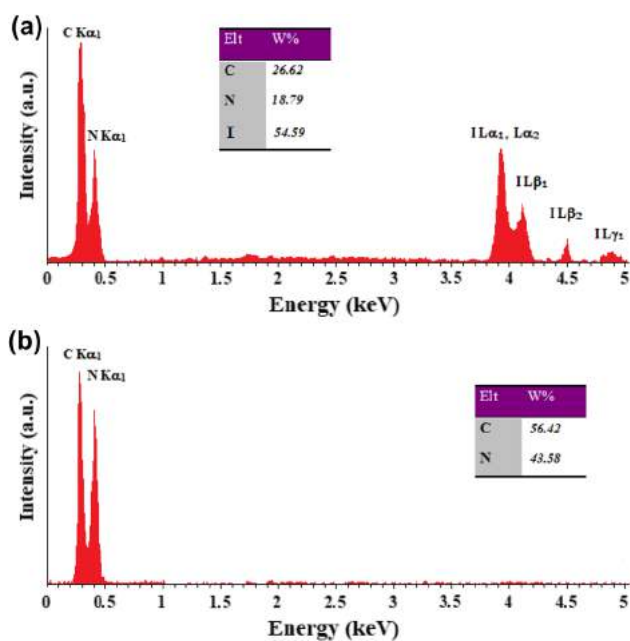
Fig. 1 EDX spectra of **a** TAIm[I] and **b** TAIm[CN] ILs

indicates the complete replacement of Cl by iodide and, sub-sequently, the formation of imidazolium iodide moieties as a result of the nucleophilic attack of methyl imidazole to the triazine framework (Fig. 1a). In the next step, the complete removal of peaks related to iodide binding energies confirms the anion exchange of [I] with [CN] (Fig. 1b). In addition, the increase in the weight percentages of C (56.42 wt%) and N (43.58 wt%) according to the Scheme 1, confirms the structure of TAIm[CN] IL. The inset tables show the weight percentages of the elements for each ionic liquid (Fig. 1).

Figure S8 shows the FTIR spectra of cyanuric iodide, TAIm[I], and TAIm[CN] IL. The peak with strong intensity at 614 cm^{-1} corresponds to the C–I stretching vibration in cyanuric iodide confirmed the successful replacement of Cl by I (Fig. S8a) [31–34]. The absorptions appearing at 2592–2929 cm^{-1} in the FTIR spectrum of TAIm[I] IL were attributed to the stretching vibrations of different modes of the imidazole rings (Fig. S8b). Also, the elimination of C–I stretching vibrations in TAIm[I] IL spectrum also confirmed the replacement of iodide with methyl imidazole. Figure S8c confirmed the formation of the TAIm[CN] IL with a very strong intensity absorption at 2098 cm^{-1} related to C≡N

stretching vibration, which was created through the replace-ment of the [CN] anion with iodide (Fig. S8c). Also, the structure of the ILs were characterized by NMR analyses. Figure S9 shows the resulting ^{1}H- and ^{13}C-NMR spectra of TAIm[I] and TAIm[CN] ionic liquids, that was confirmed the successful exchange of iodide by 1-methyl imidazole groups in the triazine framework by the corresponding peaks at 7.7–7.9 ppm related to the H–C=C–H bonds in the imi-dazolium moieties in TAIm[I]. These peaks were shifted to 8.0–8.3 ppm demonstrated the counter anion exchange of [I] by [CN] (Fig. S9c).

Figure S10 shows the FTIR spectra of Mn/TEMPO-doped Fe$_3$O$_4$ NPs and TEMPO/Fe$_3$O$_4$ NPs. A strong absorption band at 570 cm^{-1} was related to the Fe–O stretching vibra-tions in the NPs [1, 38, 39]. The vibrations that appeared in the range of 1732–1400 cm^{-1} indicate the presence of organic groups (including TEMPO/Salen moieties) in the NPs framework. These vibrations had been completely removed in Mn$_2$O$_3$-doped Fe$_3$O$_4$ NPs FTIR spectrum after heat treatment, which confirms their role as a reduction of iron ions and the formation of the corresponding nanoparti-cles. The absorptions appearing at less than 550 cm^{-1} were also attributed to Mn–O and Fe–O–Mn vibrational modes [19]. Also, a broad peak at 3300 cm^{-1} that was assigned to the adsorbed water on the NPs surfaces as well as Fe–OH (O–H stretching vibration) groups [1, 21, 29].

Table 2 shows the surface characteristics of the NPs including specific surface area, pore volume, and average pore radius using BET method. According to the results, Mn/TEMPO-doped Fe$_3$O$_4$ and Mn$_2$O$_3$-doped Fe$_3$O$_4$ NPs have a specific surface area equal to 246 m^2 g^{-1} and 641 m^2 g^{-1}, respectively. The significant increase in the specific surface area as well as the increase in the average pore radius up to 5.6 nm indicate the formation of a porous structure for Mn$_2$O$_3$-doped Fe$_3$O$_4$ NPs. In addition, the pore volume also increased from 0.320 to 1.746 cm^3 g^{-1} compared to Mn/TEMPO-doped Fe$_3$O$_4$ NPs (Table 2). The obtained pore volume for Mn$_2$O$_3$-doped Fe$_3$O$_4$ NPs was found to be higher than known porous materials like zeolites (between 0.7 and 1.3 cm^3 g^{-1}) [40], and most of metal organic frameworks (0.2–1.0 cm^3 g^{-1}) [41].

These changes were completely consistent with the ther-mal removal of TEMPO-Salen organic groups as a reducing agent, and the formation of a highly porous structure for Mn$_2$O$_3$-doped Fe$_3$O$_4$ NPs.

Table 2 Surface characteristics of Mn/TEMPO-doped Fe$_3$O$_4$ and Mn$_2$O$_3$-doped Fe$_3$O$_4$ NPs

Entry	Sample	Specific surface area (m^2 g^{-1})	Pore volume (cm^3 g^{-1})	Average pore radius (nm)
1	Mn/TEMPO-doped Fe$_3$O$_4$	246	0.320	1.004
2	Mn$_2$O$_3$-doped Fe$_3$O$_4$ NPs	641	1.746	5.642

In order to determine the amount of Mn-doped into the nanoparticles framework, EDX analysis (average of five points) and ICP analysis were used. As shown in Fig. 2a, Mn/TEMPO-doped Fe_3O_4 and Mn_2O_3-doped Fe_3O_4 NPs contain 8 wt% and 10.2 wt%Mn respectively, which indicates the successful doping of Mn in the Fe_3O_4 structure. In order to confirm the results, 10 mg of Mn/TEMPO-doped Fe_3O_4 and Mn_2O_3-doped Fe_3O_4 NPs were digested in H_2SO_4:HCl mixture and then analyzed by ICP. Based on the ICP analysis, 8.016 wt% and 10.342 wt% Mn was determined in Mn/TEMPO-doped Fe_3O_4 and Mn_2O_3-doped Fe_3O_4 NPs, respectively, which was completely consistent with the EDX analysis. The EDX analysis for these nanoparticles was shown in Fig. 2. The presence of elements such as C (21.14 wt%) and N (4.55 wt%) in the EDX spectrum of Fe_3O_4/TEMPO NPs confirmed the presence of organic groups related to TEMPO as a reducing agent and capping agent in the structure of the NPs (Fig. 2b). The C/N wt% ratio was also completely consistent with the Salen-TEMPO ligand groups in the structure of Fe_3O_4/TEMPO NPs. The complete removal of C and N peaks at about 0.3 and 0.4 keV respectively, in Mn_2O_3-doped Fe_3O_4 NPs EDX spectrum, confirms the removal of organic groups as a template and also the formation of Mn_2O_3-doped Fe_3O_4 NPs, in agreement with the results of other analyses.

The TEM images obtained from the nanoparticles showed a homogeneous morphology along with their narrow size distribution (Fig. 3). Considering that the magnetic nanoparticles are not coated with silicate or polymeric compounds, however, no significant agglomeration can be seen in the particles. As shown in the figure, the NPs have an average size of about 60 nm. The TEM image with higher resolution in the figure (Fig. 3c, inset image), also clearly shows the porosity of the nanoparticles along with the doped Mn_2O_3 nanoparticles (darker points).

Almost similar particle size distribution was obtained for Mn/TEMPO-doped Fe_3O_4 and Mn_2O_3-doped Fe_3O_4 NPs. As shown in Fig. 4A, the NPs have almost narrow and homogeneous size distribution and most of the particles have an average diameter of 60 nm (Fig. 4A).

Zeta potential measurement was studied to determine the stability and net surface charge of the NPs in deionized water. Examining zeta potential measurements for the NPs showed that the value of zeta potential for Mn/TEMPO-doped Fe_3O_4 and Mn_2O_3-doped Fe_3O_4 NPs was −22 mV and −15 mV, respectively (Fig. 4B). Considering that both of the NPs were completely spherical and have the same size distribution and average size, this shift of zeta potential towards positive values can be directly attributed to the removal of organic groups including TEMPO and Salen ligand moieties. The results have shown that the surface charge on metal oxides is due to the processes including hydration, protonation, and deprotonation of surface groups in aqueous solutions [37], which the presence of doped Mn centers in the structure of Mn/TEMPO-doped Fe_3O_4 NPs caused the increase of zeta potential (shifts towards positive values). However, by removing organic groups from Mn/TEMPO-doped Fe_3O_4 NPs, more Fe–OH groups are created on the surface and pores of Mn_2O_3-doped Fe_3O_4 NPs, which affects the shift of zeta potential towards positive values. These changes were in agreement with the previous reports on the effect of surface modification of porous nanomaterials on zeta potential [42, 43]. The presence of OH groups (resulting from the surface modifications) on the surface of the NPs causes the zeta potential to become more positive [44]. From this point of view, the removal of these organic groups also caused the particle size distribution in Mn_2O_3-doped Fe_3O_4 to shift towards smaller diameters (Fig. 4B-b). Nevertheless, the NPs still have a negative zeta potential of –15 mV. The negative zeta potential ensures the stability of the NPs in the reaction environment and prevents agglomeration.

Figure 5a shows the X-ray diffraction pattern for Mn/TEMPO-doped Fe_3O_4 and Fe_3O_4/TEMPO NPs. The presence of eight characteristic peaks at $2\theta = 30.2°$, 35.8°, 36.6°,
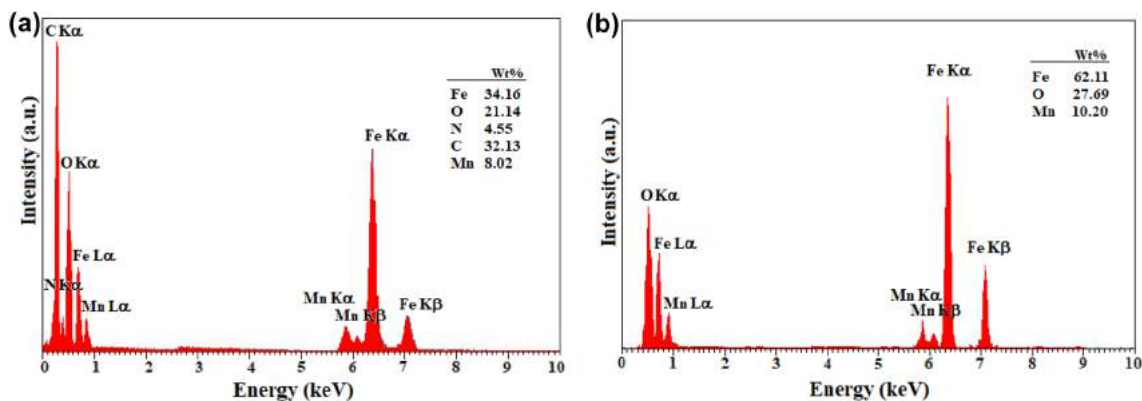
Fig. 2 EDX analyses of **a** Mn/TEMPO-doped Fe_3O_4 NPs and **b** Mn_2O_3-doped Fe_3O_4 NPs
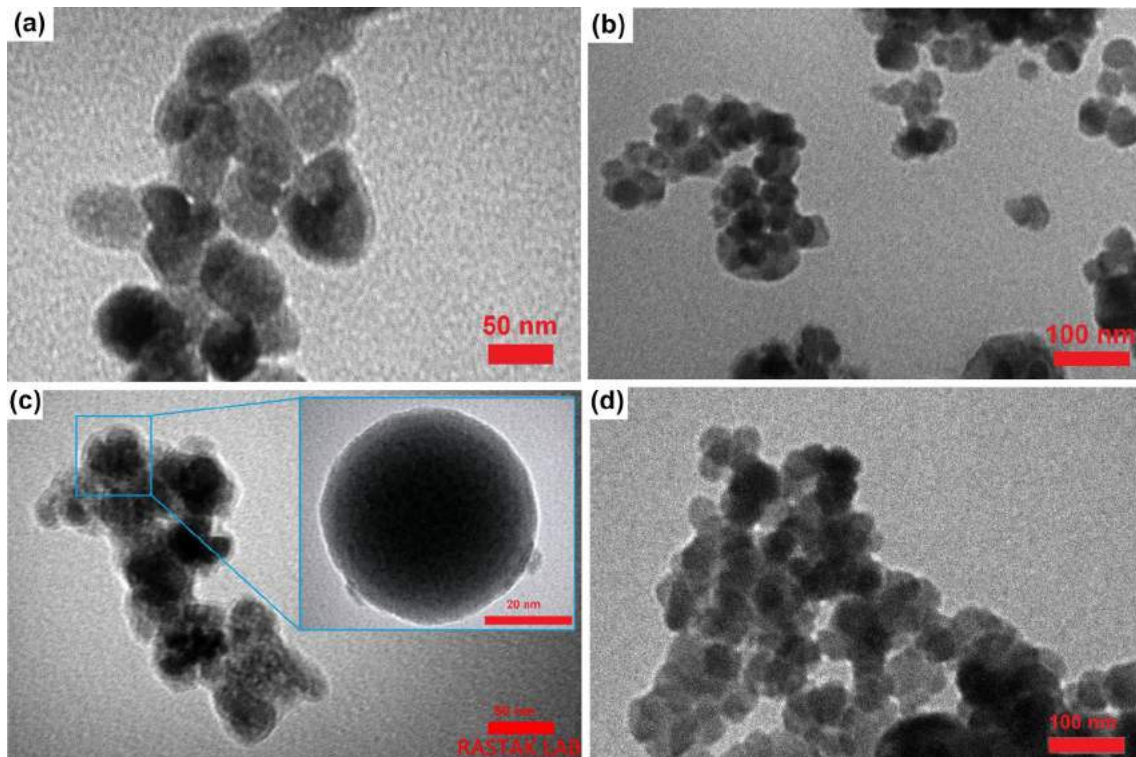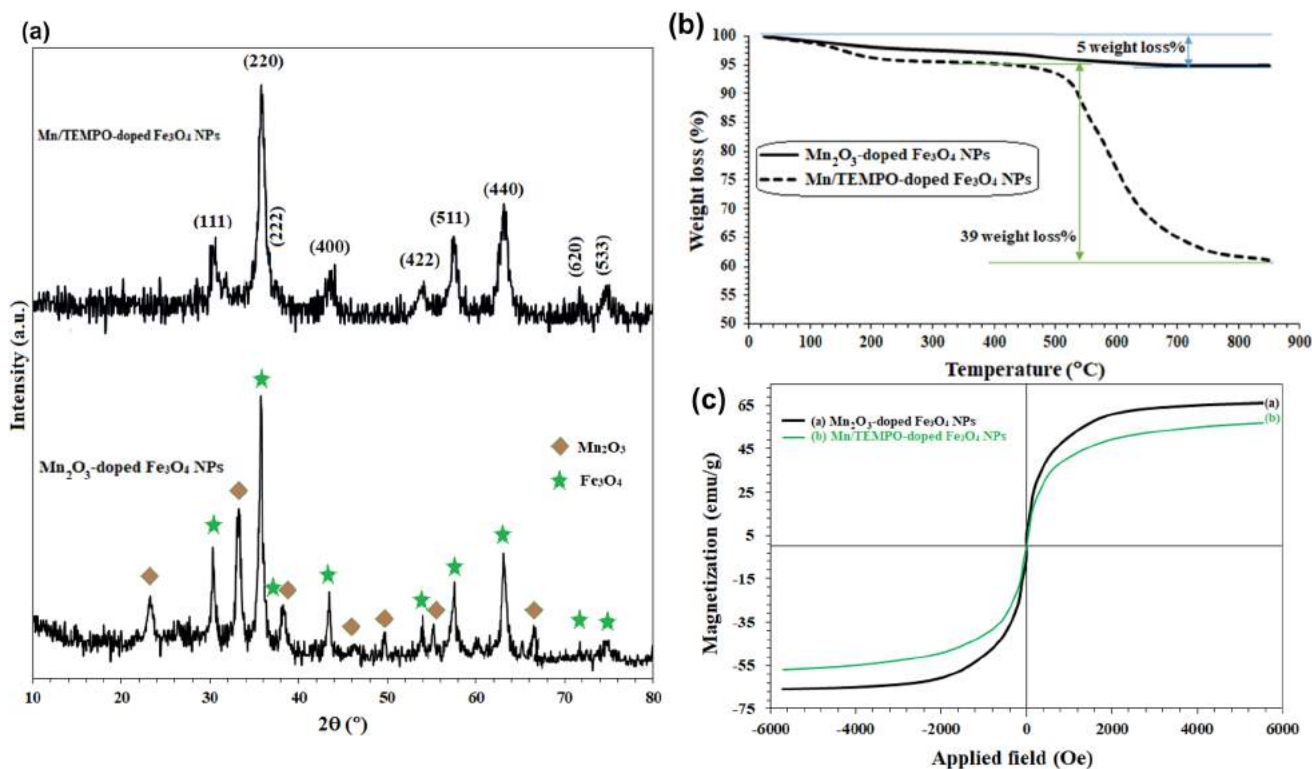
Fig. 3 TEM image of **a**, **b** Mn/TEMPO-doped Fe$_3$O$_4$ NPs and **c** and **d** Mn$_2$O$_3$-doped Fe$_3$O$_4$ NPs. The inset figure in **c** represents a single nano-particle of Mn$_2$O$_3$-doped Fe3O4 NPs with a 20 nm scale bar
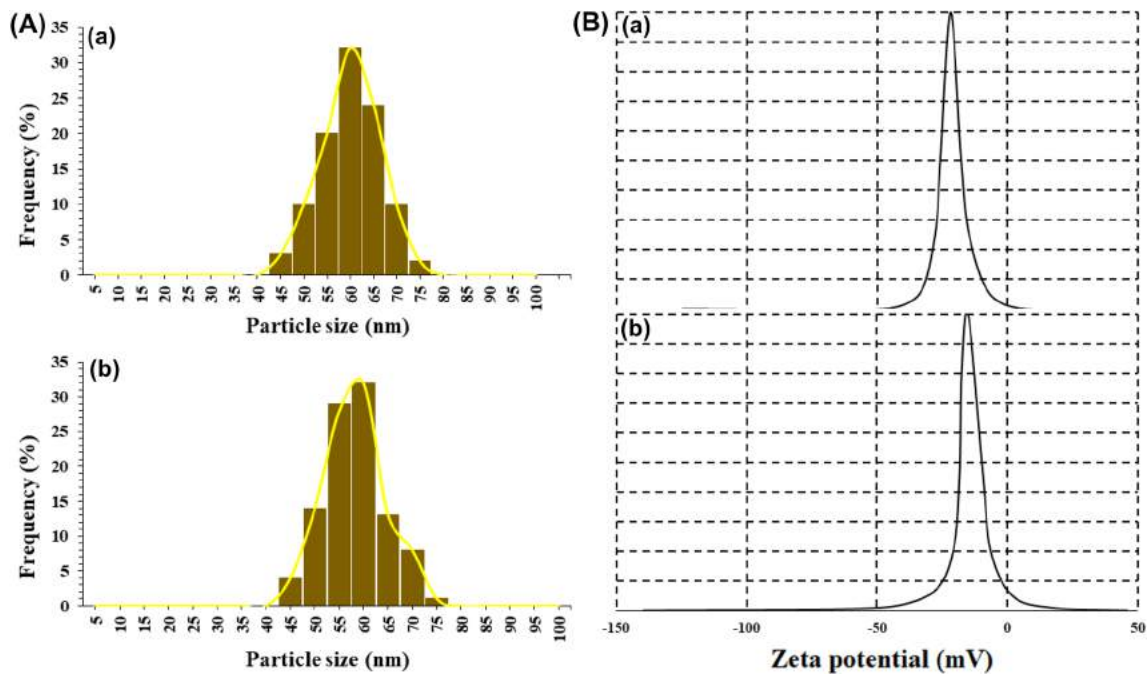
Fig. 4 **A** Size distribution of (**a**) Mn/TEMPO-doped Fe$_3$O$_4$ and (**b**) Mn$_2$O$_3$-doped Fe$_3$O$_4$ NPs obtained by DLS method. **B** Zeta potential analyses of (**a**) Mn/TEMPO-doped Fe$_3$O$_4$ and (**b**) Mn$_2$O$_3$-doped Fe$_3$O$_4$ NPs

Fig. 5 **a** XRD patterns (stars represent Fe$_3$O$_4$ phases, diamonds represent Mn$_2$O$_3$ Phases), **b** TGA curves, and **c** VSM analyses of TEMPO/Fe$_3$O$_4$ and Mn$_2$O$_3$-doped Fe$_3$O$_4$ NPs

43.0°, 53.8°, 56.6°, and 63.0° corresponding to the planes (111), (220), (222), (400), (422), (511), (440) respectively, confirming the crystal structure of Fe$_3$O$_4$ NPs in agreement with previous reports (JCPDS No.74-2402) [1, 38, 45]. XRD pattern of Mn$_2$O$_3$-doped Fe$_3$O$_4$ NPs clearly confirmed the Mn$_2$O$_3$ phases with the observed diffraction peaks at $2\theta = 23.27°$, 33.10°, 38.45°, 45.33°, 49.45°, 55.23°, and 65.90° correspond to the (211), (222), (400), (332), (431), (440), and (622) planes respectively, completely in agreement with the crystal structure of Mn$_2$O$_3$ NPs, doped in the Fe$_3$O$_4$ NPs [46]. Also, no evidence corresponding to phases such as MnO$_2$, Mn$_3$O$_4$, and MnO (and even metallic Mn) was observed in the X-ray diffraction pattern, which suggests the in situ formation of Mn$_2$O$_3$ NPs in accordance with the previous reports [19, 46]. The peaks related to Fe$_3$O$_4$ crystalline phase were also completely visible in the X-ray diffraction pattern of Mn$_2$O$_3$-doped Fe$_3$O$_4$ NPs, which confirms that the crystal structure of the Fe$_3$O$_4$ NPs remains intact after the heat treatment.

Figure 5b shows the thermal behavior of Mn/TEMPO-doped Fe$_3$O$_4$ and Mn$_2$O$_3$-doped Fe$_3$O$_4$ NPs, wherein their thermal decomposition takes place in one step. As shown in Fig. 5b, the total weight loss of 39% in the thermal decomposition of Mn/TEMPO-doped Fe$_3$O$_4$ indicates the role and the presence of doped Mn-Salen complex groups

as a reducing agent. The thermal behavior of the NPs well reflects the preparation of Mn$_2$O$_3$ NPs through the thermal decomposition of doped organic groups in the Fe$_3$O$_4$ framework. The results have shown well that the thermal decomposition of Schiff base complexes causes the formation of metal oxide NPs [21–23]. As shown in Fig. 5b, Mn$_2$O$_3$-doped Fe$_3$O$_4$ NPs have remarkable thermal stability up to about 900 °C and only 5% weight loss was observed. Also, high thermal stability was observed for Mn/TEMPO-doped Fe$_3$O$_4$ NPs. Schiff base metal complexes are known as heat-resistant compounds [47]. Furthermore, these weight losses had a correlation with the results of EDX (decomposition of organic groups with the sum of C, N wt% elements) (Fig. 2). These results also confirm the Mn doping in the crystal structure of Mn/TEMPO-doped Fe$_3$O$_4$ NPs and also the presence of organic groups in the structure of the NPs, in agreement with the results of EDX. Weight loss of 2–3 wt% between temperatures of 120–220 °C indicates the removal of water adsorbed on the surface as well as the escape of water trapped in the crystalline structure of the NPs (Fig. 5b) [1]. As shown in Fig. 5b, the thermal decomposition of Mn/TEMPO-doped Fe$_3$O$_4$ NPs takes place with a gentle slope with a wide and high temperature range (490–770 °C). On the other hand, no significant weight loss was observed for Mn$_2$O$_3$-doped Fe$_3$O$_4$ NPs, which reflects the complete

decomposition of the doped organic groups and its transformation into Mn$_2$O$_3$ NPs centers [48] in the Fe$_3$O$_4$ NPs framework, as well as the high stability of the NPs.

The results clearly show the superiority of the thermal stability of these NPs compared to when the NPs were coated with organic polymers [38, 49, 50], which due to successive coatings of polymeric compounds on the surface of the magnetic NPs undergo thermal decomposition at low temperatures and subsequently, the catalytic activity decreases.

Another advantage of the presented method was the preparation of the catalytic NPs with minimal loss of magnetic properties. Consecutive polymeric coatings on magnetic NPs surface cause a decrease in the magnetic property of the core and act as a barrier against the external magnetic field (due to simple dilution of the superparamagnetic Fe$_3$O$_4$ core with the diamagnetic complex [49]); While in the present method, the in-situ doping of Mn species in Fe$_3$O$_4$ NPs was prepared without the use of polymeric and silicate compounds, and therefore has stronger magnetic properties. According to the results of VSM analysis (Fig. 5c), Mn/TEMPO-doped Fe$_3$O$_4$ and Mn$_2$O$_3$-doped Fe$_3$O$_4$ NPs have a saturation magnetization equal to 57 and 66 emu g^{-1}, respectively. As shown in Fig. 5c, both nanoparticles have superparamagnetic behavior with a zero coercivity. Also, no hysterics loop was observed for its magnetization. The NPs were completely separated from the reaction mixture in an average time of less than 1 min. The removal of organic groups (in accordance with the thermal behavior of the NPs, Fig. 5b), caused an increase in the saturation magnetization in Mn$_2$O$_3$-doped Fe$_3$O$_4$ and indicates the removal of the diamagnetic barrier (Salen/TEMPO moieties).

Electronic spectra of the NPs also confirmed the doping of Mn/TEMPO and TEMPO groups in Mn/TEMPO-doped Fe$_3$O$_4$ NPs in agreement with the results of EDX (Fig. 2) and TGA (Fig. 5b) analyzes. As shown in Fig. 6A, a shoulder appearing at 425 nm represents the $\pi \rightarrow \pi^*$ transitions in [TEMP=O]$^+$ [51, 52]. Two absorption bands at 240 nm and 360 nm were respectively attributed to the $\pi \rightarrow \pi^*$ transitions related to C=N and C=C groups (benzene groups) [53]. Also, a peak with weaker intensity (as a shoulder) at 520 nm was attributed to metal charge transfer (O of phenolate to Mn ($p\pi \rightarrow d\pi^*$)) [54, 55]. As shown in Fig. 6A, the absorptions related to the electron transitions of Salen and TEMPO groups in Mn$_2$O$_3$-doped Fe$_3$O$_4$ NPs have been eliminated and there was only one transition at 420 nm, probably related to Mn–O–Fe and also Mn–O transitions (in Mn$_2$O$_3$ phases) [56].

In order to determine the oxidation state of Mn species in Mn/TEMPO-doped Fe$_3$O$_4$ and Mn$_2$O$_3$-doped Fe$_3$O$_4$ NPs, XPS analysis of Mn2p was performed (Fig. 6B). The presence of two peaks at 642.3 eV and 653.2 eV, respectively, indicates the binding energies of Mn2p$_{3/2}$ and Mn2p$_{1/2}$, completely consistent with Mn$^{(III)}$ oxidation state [57]. Also, the energy gap for Mn2p$_{3/2}$ and Mn2p$_{1/2}$ was equal to 10.9 eV and shows that the Mn species in Mn/TEMPO-doped Fe$_3$O$_4$ NPs were often in +3 oxidation state [39, 57]. XPS Mn2p analysis of Mn$_2$O$_3$-doped Fe$_3$O$_4$ NPs also suggests the presence of Mn centers with +3 oxidation state. As shown in Fig. 6B-b, the two peaks corresponding to Mn2p$_{3/2}$ and Mn2p$_{1/2}$ have a binding energy gap equal to 11.9 eV, which was completely consistent with the gap observed for Mn(+3) species in Mn$_2$O$_3$ [44]. In addition, the broadening of peaks also shows the presence of other Mn oxidation
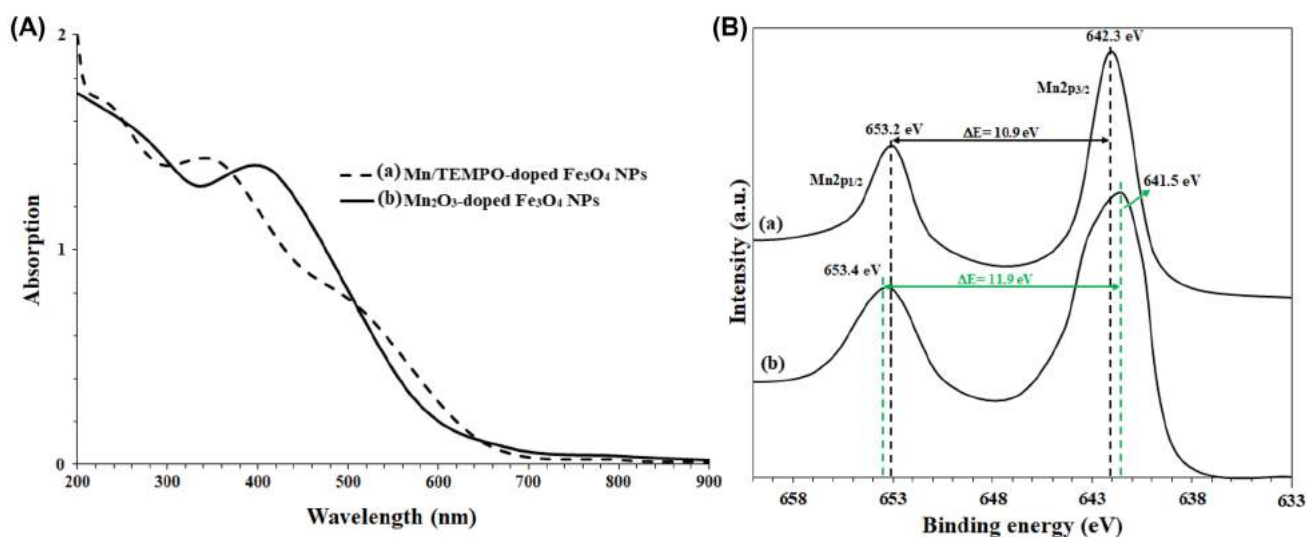

Fig. 6 **A** UV–Vis (dispersed in distilled water) and **B** High resolution XPS Mn2p (normalized, energy corrected) spectra of (**a**) Mn/TEMPO-doped Fe$_3$O$_4$ NPs and (**b**) Mn$_2$O$_3$-doped Fe$_3$O$_4$ NPs

states with lower percentages, which can be attributed to Mn–O–Fe bonds in the NPs [58, 59].

High resolution XPS-deconvulated spectra strongly confirmed the presence of the organic moieties including salen ligand and TEMPO groups in Mn/TEMPO-doped Fe_3O_4 NPs. Figure 7 shows the C 1s (Fig. 7a), N 1s (Fig. 7b), and O 1s (Fig. 7c) deconvulated spectra of Mn/TEMPO-doped Fe_3O_4 NPs. As shown in Fig. 7a, six different types of the carbon were found in the C 1s XPS spectrum. The peaks appeared at 284.5, 285.0, 286.2, 287.6, 287.8, 288.1 eV were assigned to (C–C, C–H), C–N, C=O, C=N (1), C=N (2), C=O respectively, in agreement with the literature [16, 17]. The presence of these peaks was completely related to the Mn-salen complex-doped in the NPs. The deconvulated XPS spectrum in the region of N 1s binding energies, exhibited three peaks at 398.7, 401.0, and 402.4 eV were assigned to C–N(sp^2), C–N (sp^3) and N-oxide species, respectively (Fig. 7b) [16]. The last peak with the lowest intensity confirmed the presence of doped-TEMPO groups in the structure of the NPs. Useful information was also obtained from O 1s high resolution XPS-deconvulated spectrum (Fig. 7c). Seven characteristic peaks were detected in O 1s spectrum, wherein the peaks appeared at 528.5, 528.7, 529.9, 530.2, 532.2, 530.8, and 533.4 eV, selectively were assigned to C–O, Mn–O–Fe, Fe–OH, Mn–O, Fe–O, O–Fe–O, and C–O–Fe bonds, in agreement with the literature [16, 18]. These results confirmed the doping of Mn-Salen/TEMPO moieties in Mn/TEMPO-doped Fe_3O_4 NPs. The thermal decomposition of Mn/TEMPO-doped Fe_3O_4 NPs led to the removal of peaks related to C–O–Fe and C–O–Fe binding energies in the O 1s spectrum of Mn_2O_3-doped Fe_3O_4 NPs, which confirms the removal of doped organic groups in the framework of Fe_3O_4 and the formation of Mn_2O_3 centers (Fig. 7d). In addition, the binding energies related to Fe–O, Mn–O, and Mn–O–Fe bonds were also shifted to higher energies, which indicates the creation of a more stable structure for Mn_2O_3-doped Fe_3O_4 NPs after the thermal treatment. These results also, in agreement with other results (such as TGA), suggest the formation of a stable structure for Mn_2O_3-doped Fe_3O_4 NPs.

The results of analyzes including XRD, TGA, VSM, etc. confirm the in situ preparation of Mn_2O_3 nanoparticles in the porous Fe_3O_4 structure by removing the organic template. Briefly, the presence of vibrations at 1732–1400 cm^{-1} by FTIR analysis indicate the presence of organic groups (including TEMPO/Salen moieties) in the NPs framework,
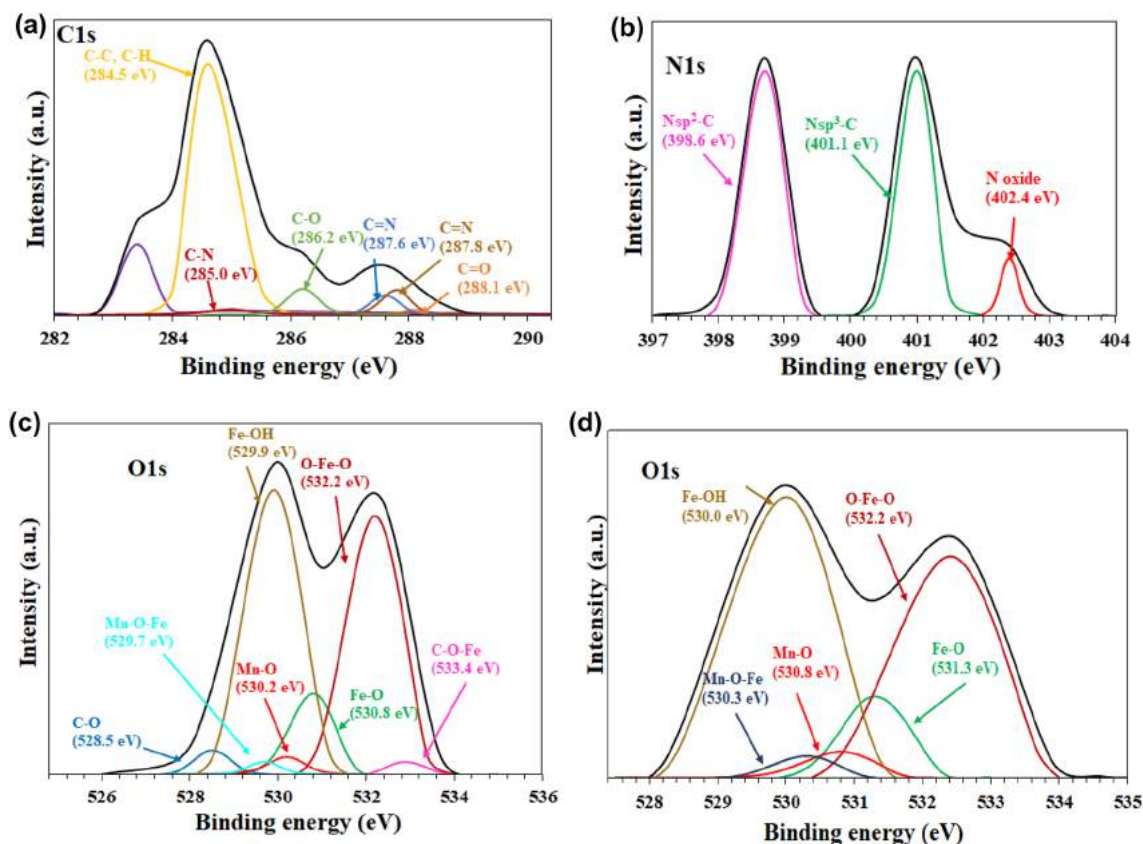
Fig. 7 Deconvulated high resolution of **a** C 1s, **b** N 1s, and **c** O 1s XPS analyses of Mn/TEMPO-doped Fe_3O_4 NPs. Deconvulated high resolution of O 1s XPS analyses of Mn_2O_3-doped Fe_3O_4 NPs

that was removed after the heat treatment and confirmed by the removal of the corresponding vibrations. Considerable increase of the pore volume from 0.320 to 1.746 cm^3 g^{-1} compared to Mn/TEMPO-doped Fe₃O₄ NPs that was consistent with creating holes in a porous structure. The complete removal of C and N peaks in the Mn₂O₃-doped Fe₃O₄ NPs EDX spectrum, confirms the removal of organic groups as a template and also the formation of Mn₂O₃-doped Fe₃O₄ NPs. XRD pattern of the NPs was completely in agreement with the crystal structure of Mn₂O₃ NPs, doped in the Fe₃O₄ NPs. More importantly, 39% weight loss and increase in the saturation magnetization in Mn₂O₃-doped Fe₃O₄ NPs compared to Mn/TEMPO-doped Fe₃O₄ NPs respectively characterized by TGA and VSM analyzes, confirm the removal of organic groups from the structure of nanoparticles. Finally, the formation of Mn₂O₃ centers was confirmed by the corresponding Mn–O–Fe and Mn–O bonds that was confirmed by the high resolution O1s XPS analysis.

3.2 Studies Over Reaction Parameters

Figure 8 shows the results of the effect of three effective parameters in the preparation of 2-phenyl-2-(phenylamino) acetonitrile (**13a**) and 2-phenyl-2-(phenylamino) propanenitrile (**15e**) including the amount of catalyst, solvent, and O₂ flow rate volume. 1-Phenylethanol (2° alcohol) was converted to the corresponding α-aminonitriles product under harsher conditions and longer time than benzyl alcohol (1° alcohol). The reaction time of 50 min and 4 h were taken to report efficiencies for **13a** and **15a**, respectively. Figure 8a shows that the highest efficiency for **13a** as well as **15a** was obtained in the amount of 2 mg of Mn₂O₃-doped Fe₃O₄ NPs (0.4 mol% Mn). In the amount of 1 mg, the efficiency drops by almost 50%. Interestingly, a negligible efficiency of 7% was observed for **13a** in the absence of the catalyst, which can be directly attributed to the TAIm[CN] IL activity. It seems that TAIm[CN] IL has the ability to directly convert benzyl alcohol to 2-phenyl-2-(phenylamino)acetonitrile in the presence of molecular oxygen. However, no efficiency was observed for **15a** in the absence of the catalyst. However, these results show the effect of Mn₂O₃-doped Fe₃O₄ NPs in catalyzing the Strecker synthesis from alcohols. Investigation of the solvent parameter showed that TAIm[CN] IL provides the highest efficiency for **13a** and **15a** in the absence of NaCN reagent (Fig. 8b). Also, a similar efficiency was obtained for TAIm[I]/NaCN mixture, which indicates the in situ preparation of TAIm[CN] IL in the mixture reaction (Scheme 2). In addition, these observations showed that the
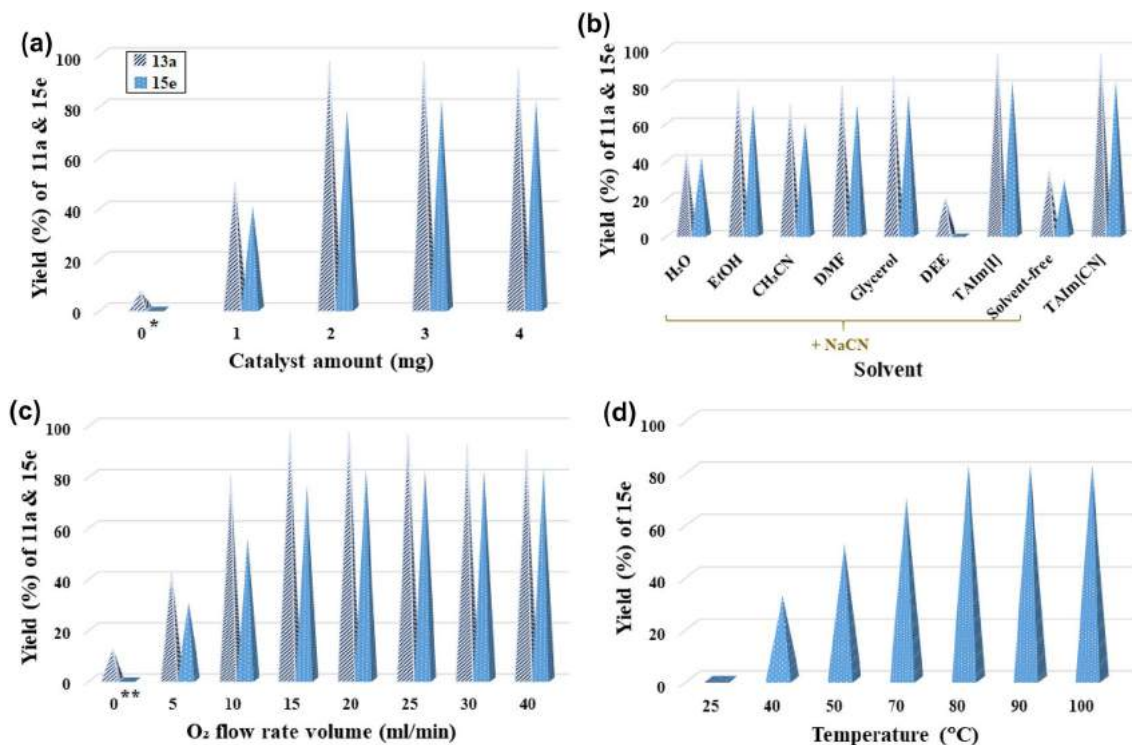
Fig. 8 Influence of **a** catalyst (Mn₂O₃-doped Fe₃O₄ NPs) amount (in TAIm[CN], O₂ (15 mL min^{-1} for **13a** and 20 mL min^{-1} for **15e**), *Catalyst-free), **b** solvent type (2.0 mL), NaCN (1.5 mmol), **c** O₂ bubbling flow rate (in TAim[CN] and 2.0 mg of Mn₂O₃-doped Fe₃O₄ NPs. **Under air atmosphere) and **d** temperature (just for **15e**) on the reaction of benzyl alcohol (1.2 mmol), aniline (1.0 mmol) for the preparation of 2-phenyl-2-(phenylamino)acetonitrile (**13a**) (at room temperature) and 2-phenyl-2-(phenylamino)propanenitrile (**15e**) at room temperature for 50 min and 4 h, respectively

efficiency of the α-aminonitrile product was independent of the amount of [CN] anion in the reaction mixture. Solvents such as glycerol (85%), DMF (80%), and CH_3CN (78%) gave moderate yields for **13a** in the presence of NaCN. Water and DEE produced the lowest efficiency for **13a**. Finally, a low efficiency equal to 35% and 30% were obtained for **13a** and **15a**, respectively under solvent-free conditions at room temperature (Fig. 8b).

Also, a similar trend with lower efficiencies was observed for **15a**. Investigating the effective parameter of O_2 flow rate volume (as bubbling) as an oxidizing agent, showed that at a flow rate of 15 mL min^{-1}, the highest efficiency was achieved for **13a** (Fig. 8c). As shown in Fig. 8c, in the absence of molecular oxygen (in air), 12% isolated yield was observed for **13a**, indicating the high catalytic activity of Mn_2O_3-doped Fe_3O_4 NPs even under air atmosphere, for the oxidation of benzyl alcohols and their subsequent conversion to α-aminonitriles. At flow rate volume higher than 40 mL min^{-1}, the efficiency decreased slightly, but at flow rate volumes lower than 15 mL min^{-1}, the efficiency decreased exponentially. But for **15e**, the highest efficiency was obtained at a flow rate of 20 mL min^{-1}, and no efficiency was observed under air atmosphere (Fig. 8c). At room temperature, the highest efficiency was obtained for **13a** (97%).

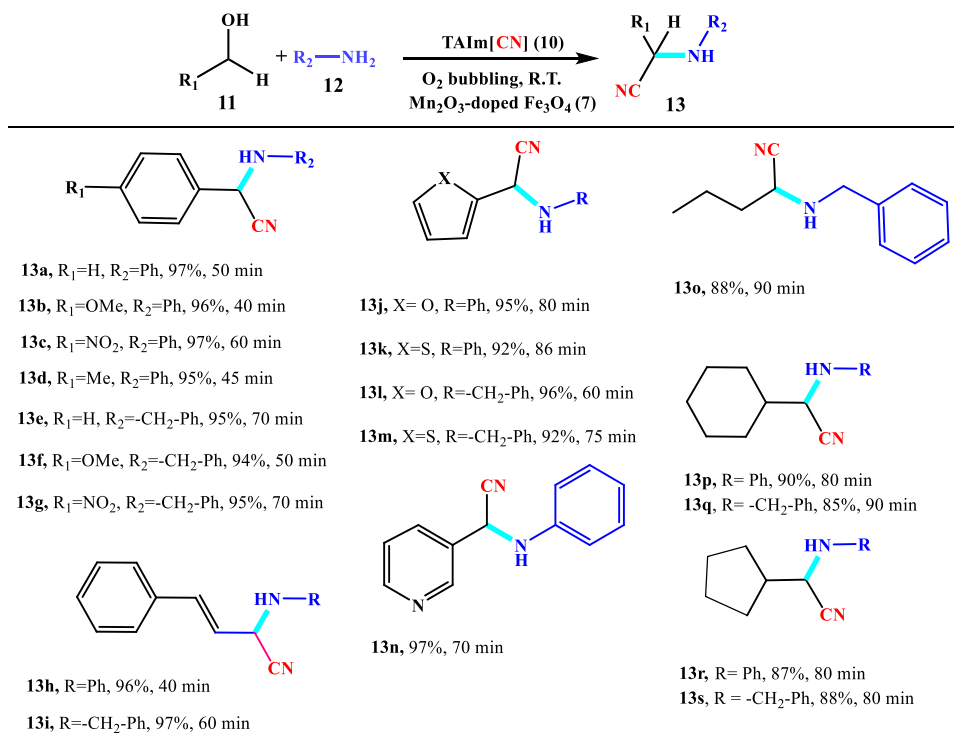At room temperature, the highest efficiency was obtained for **13a** (97% isolated yield). For **15e**, the highest possible efficiency at 80 °C (in TAIm[CN] IL) equal to 82% isolated yield was obtained. A further increase in temperature did not affect the efficiency of **15e**, but at temperatures below 80 °C, the efficiency decreased significantly. No efficiency was observed for **15e** at room temperature.
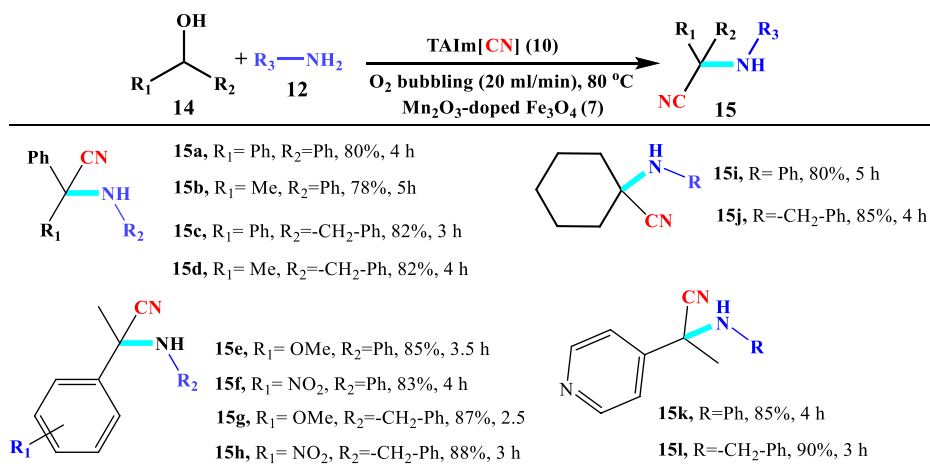
3.3 Catalytic Activity

The catalytic activity of Mn_2O_3-doped Fe_3O_4 NPs was evaluated in order to prepare α-aminonitriles from 1° and 2° alcohols in the presence of TAIm[CN] IL as an effective reagent for the [CN] transfer as well as an effective solvent. Table 3 shows these results for 1° alcohols. According to the results, the presented method has high compatibility with aniline and benzyl amines as well as benzyl, aliphatic and heterocyclic alcohols. The efficiency for aromatic alcohols (e.g. **13a**-**13g**) was higher than heterocyclic alcohols (**13j**-**13m**) and also aliphatic alcohols (**13o**-**13s**). However, for all derivatives, high to excellent yields (80–97%) was obtained for 40–90 min. Also, consistent with the results, aniline gave better yields than benzylamine (compare e.g. **13a** with **13e**, **13b** with **13f**, and **13c** with **13g**).

Next, the ability to convert 2° alcohols to α-aminonitriles was evaluated. Table 4 shows the efficiency of various derivatives of 2° alcohols including 1-phenylethanols, cyclohexanol, diphenylmethanols, and 4-(1-hydroxyethyl)pyridine to

Table 3 Mn_2O_3-doped Fe_3O_4 catalyzed Strecker synthesis of aryl amines with 1° alcohols

13a, R₁=H, R₂=Ph, 97%, 50 min
13b, R₁=OMe, R₂=Ph, 96%, 40 min
13c, R₁=NO₂, R₂=Ph, 97%, 60 min
13d, R₁=Me, R₂=Ph, 95%, 45 min
13e, R₁=H, R₂=-CH₂-Ph, 95%, 70 min
13f, R₁=OMe, R₂=-CH₂-Ph, 94%, 50 min
13g, R₁=NO₂, R₂=-CH₂-Ph, 95%, 70 min

13h, R=Ph, 96%, 40 min
13i, R=-CH₂-Ph, 97%, 60 min

13j, X=O, R=Ph, 95%, 80 min
13k, X=S, R=Ph, 92%, 86 min
13l, X=O, R=-CH₂-Ph, 96%, 60 min
13m, X=S, R=-CH₂-Ph, 92%, 75 min

13n, 97%, 70 min

13o, 88%, 90 min

13p, R= Ph, 90%, 80 min
13q, R= -CH₂-Ph, 85%, 90 min

13r, R= Ph, 87%, 80 min
13s, R = -CH₂-Ph, 88%, 80 min

Reaction conditions: Alcohol (1.2 mmol), amine (1.0 mmol), TAIm[CN] ionic liquid (2.0 mL), Mn2O3-doped Fe3O4 NPs (2.0 mg, 0.4 mol Mn), O2-bubbling (15 mL min^{-1} flow rate volume), room temperature

Table 4 Mn$_2$O$_3$-doped Fe$_3$O$_4$ catalyzed Strecker synthesis of aryl amines with 2° alcohols

15a, R$_1$= Ph, R$_2$=Ph, 80%, 4 h

15b, R$_1$= Me, R$_2$=Ph, 78%, 5h

15c, R$_1$= Ph, R$_2$=-CH$_2$-Ph, 82%, 3 h

15d, R$_1$= Me, R$_2$=-CH$_2$-Ph, 82%, 4 h

15e, R$_1$= OMe, R$_2$=Ph, 85%, 3.5 h

15f, R$_1$= NO$_2$, R$_2$=Ph, 83%, 4 h

15g, R$_1$= OMe, R$_2$=-CH$_2$-Ph, 87%, 2.5

15h, R$_1$= NO$_2$, R$_2$=-CH$_2$-Ph, 88%, 3 h

15i, R= Ph, 80%, 5 h

15j, R=-CH$_2$-Ph, 85%, 4 h

15k, R=Ph, 85%, 4 h

15l, R=-CH$_2$-Ph, 90%, 3 h

Reaction conditions: Alcohol (1.2 mmol), amine (1.0 mmol), TAIm[CN] ionic liquid (2.0 mL), Mn2O3-doped Fe3O4 NPs (2.0 mg, 0.4 mol Mn), O2-bubbling (20 mL min^{-1} flow rate volume), 80 °C

the corresponding α-aminonitriles. As shown in the optimization studies, 2° alcohols require more stringent conditions to convert to α-aminonitriles than 1° alcohols. Also, compared to 1° alcohols, the reaction time was increased in the range of 2.5–5 h. These differences can be attributed to the steric hindrance effect of the α-carbon that affect the amine nucleophilic attack. Also, this steric hindrance affects the nucleophilic attack of [CN] anion in the reaction path. By applying a temperature of 80 °C as well as 20 mL min^{-1} O$_2$ flow rate volume, good to excellent efficiency was obtained for all substrates. As shown in Table 4, benzylamine gave a better yield than aniline from a time and efficiency standpoint (see e.g., **15a** with **15c**, **15b** with **15d**, etc.). These results can be attributed to less steric hindrance and ease of nucleophilic attack on alcohol. Probably, the proper interaction of TAIm[CN] IL with 2° alcohols (as well as the related intermediates) causes them to cross the steric hindrance barrier and 2° alcohols were also converted to the corresponding α-aminonitriles.

## 4 Control Experiments

The oxidation ability of alcohols to carbonyls, direct preparation of imines from alcohols, and conversion of imines to α-aminonitriles catalyzed by Mn$_2$O$_3$-doped Fe$_3$O$_4$ NPs were also studied. Scheme 3 shows the efficiency of these conversions. At first, the ability to oxidize benzyl alcohols by Mn$_2$O$_3$-doped Fe$_3$O$_4$ NPs was evaluated and studied under the conditions used in the preparation of α-aminonitriles. As shown in Scheme 3, benzyl alcohols were completely selectively converted to the desired aldehyde product. Considering that benzyl alcohols have the ability to create various oxidation products [34, 38, 39, 57], the selectivity of the method is of great importance. The reaction time

was between 45 and 60 min and excellent efficiencies for the resulting benzaldehydes were reported. But the direct conversion of alcohol to imine in the presence of aniline took place in a shorter time (between 30 and 40 min), and it seems that the direct conversion of alcohol to imine takes place through a different pathway (mechanism).

The results clearly show the superiority of the method of the direct conversion of alcohol to α-aminonitriles compared to the stepwise methods [60]. Due to the ability of benzyl alcohols to be oxidized by Mn$_2$O$_3$-doped Fe$_3$O$_4$ NPs, the prepared aldehydes were immediately converted into α-aminonitriles in the presence of amine and TAIm[CN] IL and were removed from the reaction environment as a solid. This causes the continuous progress of the oxidation according to Le Chatelier's principle and thus increases the efficiency of the reaction. While in the stepwise method, the nucleophilic attack of [CN] groups in TAIm[CN] seems to be more difficult to the relatively stable and strong imine bond. As will be reflected in the mechanistic studies, the conversion of alcohols to α-aminonitriles will pass through intermediates that will bypass the formation of the imine bond.

Also, in order to clarify that the catalytic activity of Mn$_2$O$_3$-doped Fe$_3$O$_4$ NPs is unique, its catalytic activity was compared with (i) Mn/TEMPO-Salen complex **4**, (ii) physical mixture of Mn(OAc)$_2$ 4H$_2$O + **2**, (iii) Mn/TEMPO-doped Fe$_3$O$_4$ NPs **6**, (iv) Mn(OAc)$_2$ 4H$_2$O, and (v) 1-oxyl (4-oxo-TEMPO) in the preparation of **13a**. Complex **4** produced only 44% yield for 50 min (Table 5, entry 1). In addition, the physical mixture of **2** with Mn salt also gave 10% yield (Table 5, entry 2). The results clearly show the catalytic effect of Mn$_2$O$_3$-doped Fe$_3$O$_4$ NPs compared to homogeneous samples, that the surface-to-volume ratio and high porosity of the NPs lead to the significant efficiencies for α-aminonitriles products (Table 5, entries 1,2).
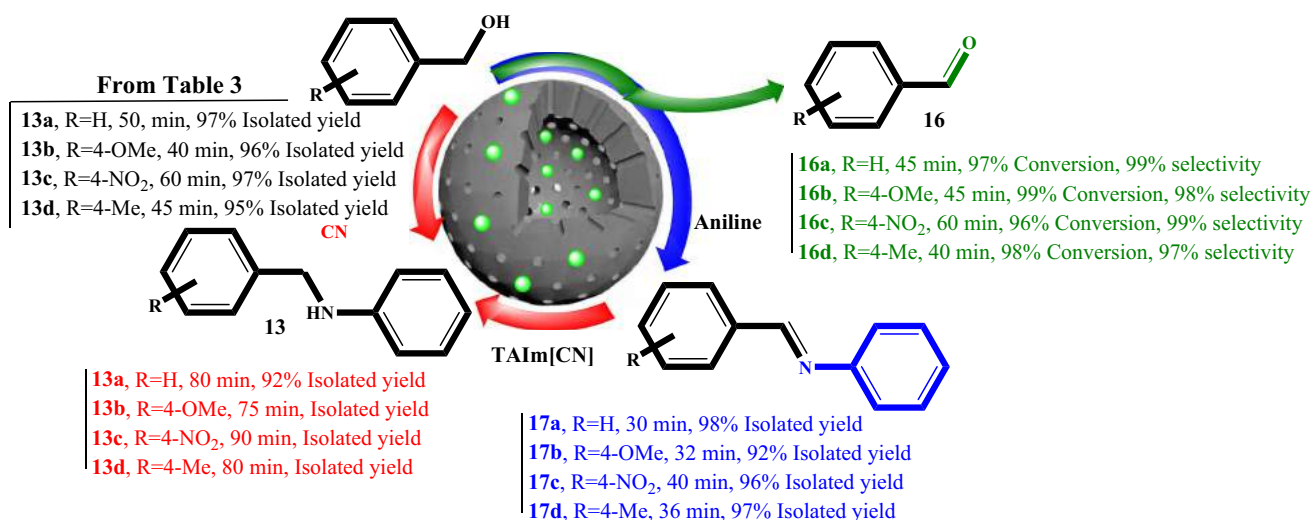
Scheme 3 Evaluation and comparison in the alcohol oxidation, direct synthesis of alcohol to imine in the presence of amine, synthesis of α-amino nitrile from amine with the direct synthesis of α-amino nitrile from alcohol catalyzed by Mn_2O_3-doped Fe_3O_4 NPs. The %conversion reported for aldehyde derivatives was reported by GC injection

Table 5 Catalytic activity of 4, 6, $Mn(OAc)_2 \cdot 4H_2O$, and 1-oxyl (4-oxo-TEMPO) over the synthesis of 13a from alcohol in the presence of TAIm[CN] ionic liquid under premium conditions

Entry	Catalyst	Time (min)	Yield (%)
1	Mn/TEMPO-Salen complex **4**	50	44
2[a]	$Mn(OAc)_2 \cdot 4H_2O + 2$	50	10
3	Mn/TEMPO-doped Fe_3O_4 NPs **6**	50	85
4	$Mn(OAc)_2 \cdot 4H_2O$	50	Trace
5	1-Oxyl (4-oxo-TEMPO)	50	Trace
6	1-Oxyl (4-oxo-TEMPO) $+ Mn(OAc)_2 \cdot 4H_2O$	50	16

[a]Physical mixture of $Mn(OAc)_2 \cdot 4H_2O$ with Schiff base ligand **2**

Nanoparticles **6** produced a relatively high efficiency of 85% for **13a**, however, the superiority of Mn_2O_3-doped Fe_3O_4 NPs compared to **6** can be attributed to the high porosity of Mn_2O_3-doped Fe_3O_4 NPs and consequently the increase in their surface to volume ratio compared to nanoparticles **6** (Table 5, entry 3). With the diffusion of the reactants into these pores containing Mn_2O_3 catalytic active centers, it causes an increase in the effective concentration in the pores and subsequently increases the efficiency of the reaction. In addition, the Mn_2O_3-doped centers in these pores have a stronger Lewis acid character [61] and improves the catalytic activity towards the preparation of α-aminonitriles.

To verify the Lewis acidity of the surface of Mn_2O_3-doped Fe_3O_4 NPs, the NPs were treated with various concentrations of pyridine as a probe molecule, and the pyridine adsorption was monitored by FTIR technique [60, 62]. Figure S11 shows the corresponding FTIR spectra. As shown in Fig. S11 advent of three characteristic peaks at 1446, 1498, and 1545 cm^{-1} demonstrated the coordinately bonded pyridine to Lewis acid sites and also pyridinium ion or H-bonded pyridine, in agreement with the literature [60, 62].

No efficiency was observed for 1-oxyl (4-oxo-TEMPO) and $Mn(OAc)_2 \cdot 4H_2O$ (Table 5, entries 4,5). Also, a physical mixture of 1-Oxyl (4-oxo-TEMPO) and $Mn(OAc)_2 \cdot 4H_2O$ gave 16% efficiency for **13a**, which reflects the unique catalytic activity of Mn_2O_3-doped Fe_3O_4 NPs (Table 5, entry 6). These control experiments showed that the characteristics such as high porosity, Mn_2O_3 active sites, and high surface-to-volume ratio have created unique catalytic properties for Mn_2O_3-doped Fe_3O_4 NPs.

5 Recyclability Studies

One of the major disadvantages of heterogeneous catalysts is their metal leaching (loss of active sites), which causes a significant drop in their catalytic activity during successive cycles. Often, the catalysts prepared based on the immobilization of transition metal complexes on nanoparticles as a substrate, undergo metal leaching, catalysis poisoning, and thermal or chemical decomposition in the reaction mixture. For this purpose, the amount of Mn leaching during successive cycles in the model reaction (Preparation of **13a**) was studied by ICP-MS analysis. This analysis was done after the end of each cycle, for ten consecutive cycles, from the remaining solution (after separating the catalyst with an external magnet). According to the results, no traces of Mn were observed in any of the residues of cycles 1th to 10th, which reflect the high stability and absence of any metal leaching of the NPs in the reaction conditions.
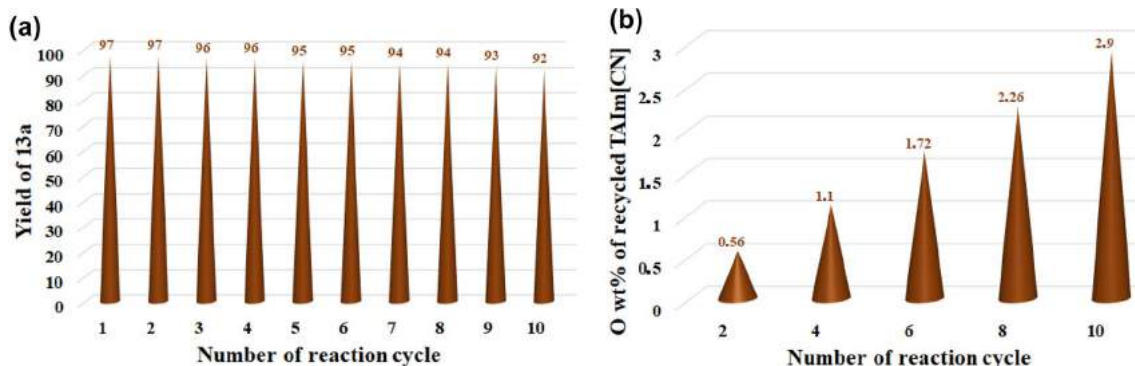
The recyclability of Mn_2O_3-doped Fe_3O_4 NPs was also studied in the model reaction of the preparation of **13a** from benzyl alcohol and aniline in the presence of TAIm[CN] IL. Figure 9a shows the results of this study for ten consecutive recovery runs. As shown in Fig. 9, a slight drop in efficiency was observed at each cycle time, so that after the end of the 10th cycle, the efficiency reduced from 97 to 92% (only 5% drop in efficiency). Considering that the catalyst does not have any metal leaching, this small amount of efficiency can be attributed to the mass loss of the NPs during successive cycles (consecutive washing and drying).

Most importantly, TAIm[CN] IL can also be recovered as an effective nitrile solvent and reagent. Also, the previous reports on this type of ILs confirm its recoverability through solvent–solvent extraction [31–34]. Due to the high water solubility of TAIm[CN] IL, it was extracted after adding EtOAc and water. In the study of elemental weight percentage composition in the recovered TAIm[CN] IL, O element was also detected (Fig. 9b). As mechanistic studies will also show, the presence of O in the TAIm[CN] IL structure can be attributed to the exchange of [CN] ions with [OH] in the reaction path, which also causes the reaction to progress. As shown in Fig. 9b, the value of O wt% increases during successive cycles, which confirms the aforementioned hypothesis. The results were completely consistent with the consumption of about 1.0 mmol of [CN] groups (corresponding to the formation of one mmol of [OH]). However, this change in the weight percentage composition of the ionic liquid did not significantly affect the efficiency of the preparation of **13a** during successive cycles, because the number of mmoles used in the reaction (2 mL, 21 mmol [CN]) was much higher than the limiting agent (aniline) and a maximum of one millimol of [CN] groups was consumed in each cycle. This phenomenon was also reflected in the proposed mechanism in accordance with the various published reports on multifunctional catalytic systems containing ionic liquids (refer to the next section). Nevertheless, treating the ionic liquid with NaCN aqueous solution causes the replacement of OH groups with CN and its reusability (see Scheme 4).

In order to investigate and study the structure of Mn_2O_3-doped Fe_3O_4 NPs, the recovered NPs in the preparation of **13a** (The direct synthesis of **13a** from benzyl alcohol and aniline in the presence of TAIm[CN] IL under the obtained optimum conditions) was washed by deionized water and ethanol after the end of the 10th cycle, and after drying, they were studied by VSM, EDX, FTIR and TEM analyses. Figure 10A shows the VSM analysis of Mn_2O_3-doped Fe_3O_4 NPs after the 10th recovery, compared to the magnetic behavior of the freshly prepared NPs. According to Fig. 10A, no significant drop or change in the magnetic behavior of the NPs was observed and both graphs almost cover each other. In addition, EDX and FTIR elemental analysis also showed the same percentage composition for the elements and structure for the NPs compared to the freshly prepared NPs. As shown in Fig. 10B and C, the NPs fully maintained their structure in successive cycles, which reflects their high stability in reaction conditions and suggests the continuous and reliable use of the NPs. Also, the nanoparticle morphology remained intact even after the ten consecutive recycles. Figure 10D shows the TEM image of the recovered NPs with the same morphology as the freshly prepared Mn_2O_3-doped Fe_3O_4 NPs (Fig. 3).

According to the results of lack of metal leaching, negligible loss of efficiency, and structural stability of the NPs up to at least 10 cycles, Mn_2O_3-doped Fe_3O_4 NPs have high structural stability, and confirm the reliable continuous use of the NPs in the long term. From this point of view, the NPs can be used as a reliable alternative to the previously reported heterogeneous catalysts for the efficient preparation of α-aminonitriles from alcohols.

Fig. 9 **a** Recyclability of Mn_2O_3-doped Fe_3O_4 NPs and **b** O wt% of the recycled TAIm[CN] by EDX analysis (mean of five points) on the direct synthesis of 13a by the reaction of benzyl alcohol and aniline in the presence of TAIm[CN] catalyzed by Mn_2O_3-doped Fe_3O_4 NPs for 50 min

Scheme 4 A plausible reaction mechanism for one-pot synthesis of α-amino nitriles from alcohol and amine catalyzed by Mn$_2$O$_3$-doped Fe$_3$O$_4$ NPs
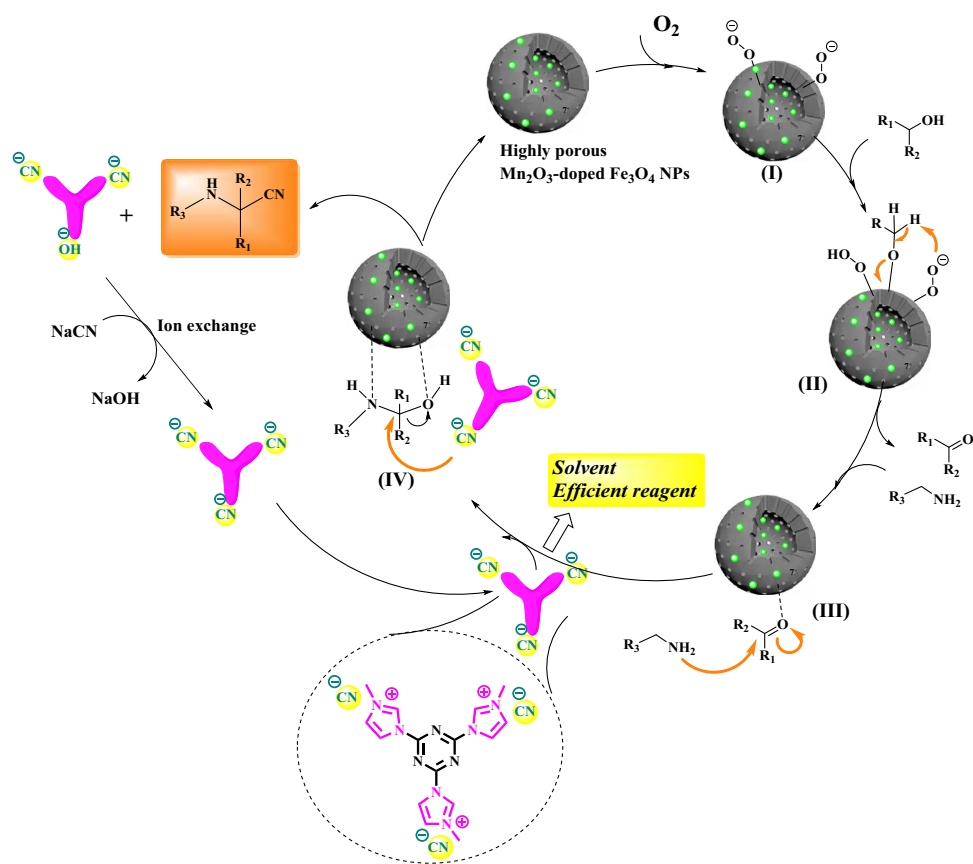
6 Mechanism Studies

Scheme 4 shows the proposed mechanism for the preparation of α-aminonitriles from alcohols in agreement with the previous reports [11, 63] and observations from control experiment, recyclability and the catalytic activity of Mn$_2$O$_3$-doped Fe$_3$O$_4$ NPs. Proof of the absence of radical species was also investigated by adding hydroquinone, as an electron scavenger/capture, once at the beginning and once after 30 min (yield = 66%) in the reaction to prepare **13a** (under optimized conditions). In order to ensure the obtained results, each test was repeated twice. The results showed that the presence of hydroquinone (whether at the beginning of the reaction or after 66% yield) has no effect on the oxidation reaction or the subsequent preparation of **13a** from aldehyde and there are no radical species in these synthetic pathways (especially stages I, II). Figure S12 shows the yield of **13a** in the absence and presence of hydroquinone at time 0 and 30 min.

The results showed that Mn$_2$O$_3$-doped Fe$_3$O$_4$ NPs have a dual function for the selective and effective oxidation of benzyl alcohols and also catalyzing the preparation α-aminonitriles. Also, the results of the control experiments showed that the direct conversion of alcohol to α-aminonitriles passes through intermediates that bypass

the formation of the imine bond. As shown in Scheme 4, at first, molecular oxygen in the presence of Mn$_2$O$_3$-doped Fe$_3$O$_4$ NPs, causes the formation of -O–O- active species on the surface of the NPs (intermediate I) [64, 65]. According to the obtained observations, the presence of molecular oxygen is crucial for the oxidation reactions and subsequent preparation of α-aminonitrile (Fig. 8c). As shown in Fig. 8c, no significant oxidation takes place under air atmosphere.

In the next step, these active species, by absorbing the alcoholic proton, help the surface adsorption of alcohols on the surface of the NPs (intermediate II). Also, the results of the pyridine test on Mn$_2$O$_3$-doped Fe$_3$O$_4$ NPs showed that the surface of the catalyst has the characteristic of Lewis acid. By proving the absence of radical species in the reaction mechanism as well as Lewis acid centers on the catalyst surface (shown on the previous section), aldehyde species are physically adsorbed on the catalyst surface.

By the benzylic proton abstraction by the –O–O– active groups (adsorbed on the surface of the NPs), the aldehyde product was formed. In the presence of amine reactant, nucleophilic attack was provided for the adsorbed aldehydes (via aldehyde oxygen) on the surface of the NPs (intermediate III) and formation of intermediate IV. TAIm[CN] IL acts not only as a solvent but also as an effective reagent to transfer [CN] to intermediate IV. As shown in Scheme 4,
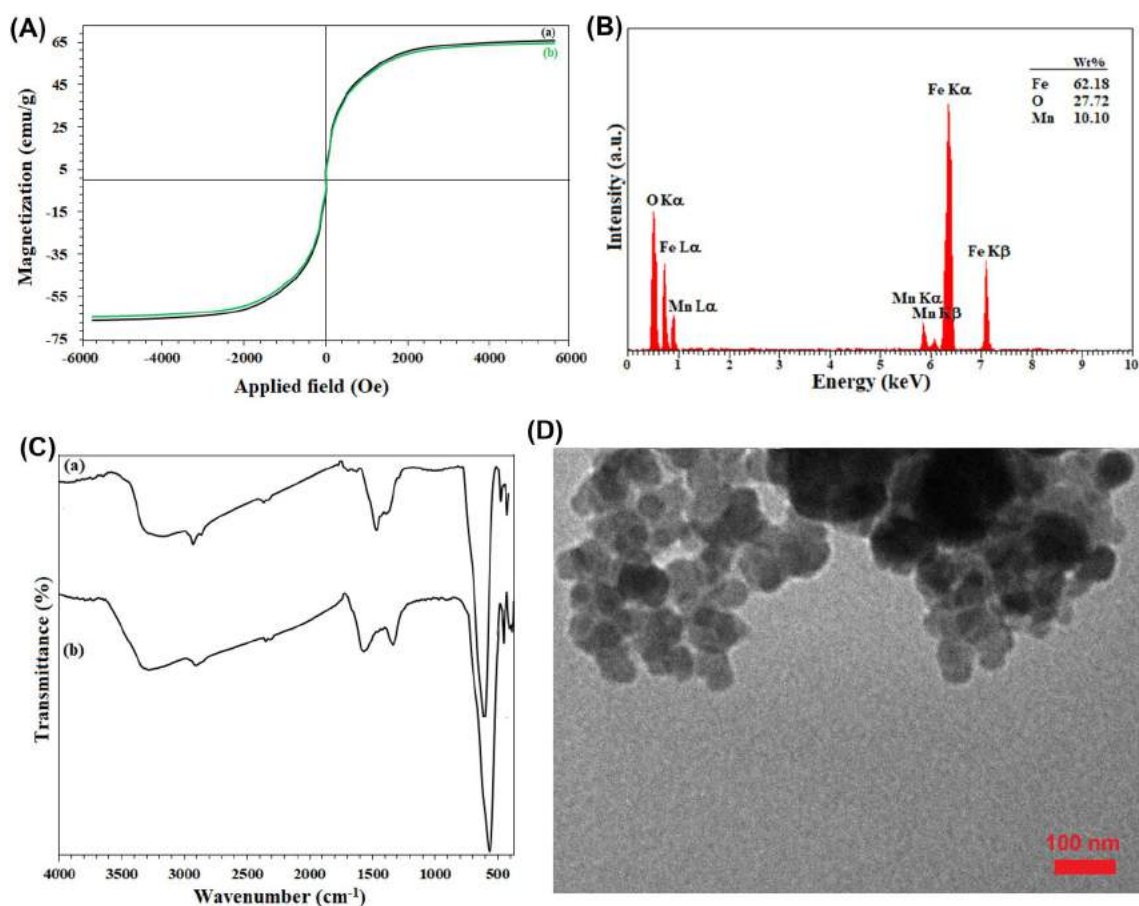
Fig. 10 **A** VSM analyses and **C** FTIR spectra of (**a**) the freshly prepared and (**b**) the reused Mn$_2$O$_3$-doped Fe$_3$O$_4$ NPs after 10th run. **B** EDX spectrum and **D** TEM image of the reused Mn$_2$O$_3$-doped Fe$_3$O$_4$ NPs after 10th run

nucleophilic attack of the [CN] counter anion in TAIm[CN] IL leads to the formation of the desired α-aminonitrile. Previously, Kazemnejadi et al. showed the similar participation of [CN] ions in a bifunctional catalyst containing [CN] counter anions (in ionic liquid moieties) [1]. The OH groups separated from intermediate IV were also absorbed by TAIm[CN] IL and the catalyst returns to the cycle again. The presence of oxygen element in the recovered ionic liquid (from EDX analysis, Fig. 2b) confirms this process (Scheme 4). This anion exchange was also shown in multifunctional catalysts bearing ionic liquids in the transesterification and aldol condensation reactions [31], C–C coupling [31], preparation of tetrazole compounds [33], and oxidation of alcohols [34]. Also, TAIm[CN, OH] IL returns to its original form after being treated with aqueous solution of NaCN and can be used again. As shown in the recovery studies (Figs. 9, 10), TAIm[CN] IL without any treatment can be used up to 10 consecutive times without loss of activity, and exchange of [CN] with [OH] had no effect on its activity or solubility. As mentioned earlier, an explanation for this stability could be the very high concentration of [CN] in the

reaction mixture, which caused it to be independent from the reaction rate (about 1 mmol of [CN] groups were consumed in each cycle). However, Scheme 4 only shows the recyclability of TAIm[CN] IL in order to sustain the environment and economic efficiency.

7 Conclusion

This paper introduces a novel strategy for the synthesis of highly porous Mn$_2$O$_3$-doped Fe$_3$O$_4$ NPs with high catalytic activity. The sodium salt of the asymmetric Mn/TEMPO-Salen complex was found as an efficient reducing agent and template to reduce Fe ions (Fe^{2+}, Fe^{3+}) to synthesis of Mn/TEMPO-doped Fe$_3$O$_4$ NPs as precursor for the subsequent preparation of Mn$_2$O$_3$-doped Fe$_3$O$_4$ NPs via the thermal decomposition. Mn$_2$O$_3$-doped Fe$_3$O$_4$ NPs was found as an efficient, highly porous and thermal stable recyclable nanocatalyst for the efficient transformation of alcohols 1° and 2° to the corresponding α-aminonitriles via the Strecker synthesis. The surface characteristic studies of the NPs revealed

that the specific surface area, pore volume, and average pore radius of the NPs were equal to 641 m^2 g^{-1}, 1.746 cm^3 g^{-1}, and 5.642 nm respectively, which was completely consistent with the high porous NPs. The NPs showed a dual functionality of (i) selective oxidation of alcohols to carbonyls in the presence of molecular O$_2$, and (2) transformation of the corresponding carbonyls (aldehydes and ketones) to the α-aminonitriles in the presence of recyclable TAIm[CN] IL, as an efficient solvent and CN-reagent. High to excellent yields were achieved at room temperature for 1° alcohols and at 80 °C for 2° alcohols. Mn$_2$O$_3$-doped Fe$_3$O$_4$ NPs could be used for the selective oxidation of alcohol to carbonyls, direct synthesis of imines from alcohols, and the efficient transformation of carbonyls to α-amino nitriles. TAIm[CN] could be recycled (for at least 10 consecutive runs) from the reaction medium by simple solvent–solvent extraction and reused for several times after treatment with NaCN, without any loss of activity in terms of solvent and nitrile suppler properties. Also, Mn$_2$O$_3$-doped Fe$_3$O$_4$ NPs could be recycled for at least 10 consecutive cycles in the Strecker synthesis with preservation of the catalytic activity and structural/physical properties that was confirmed by VSM, EDX, FTIR, and TEM analyses.

Supplementary Information The online version contains supplementary material available at https://doi.org/10.1007/s10562-022-04210-0.

Declarations

Conflict of interest The authors declare that they have no conflict of interest.

References

1. Kazemnejadi M, Alavi SA, Rezazadeh Z, Nasseri MA, Esmaeilpour M, Allahresani A (2020). Appl Organomet Chem. https://doi.org/10.1002/aoc.5273
2. He Z, Feng L, Wu P, Li S, Kazemnejadi M (2020) ChemistrySelect 5:7753–7767
3. Ezzatzadeh E, Hossaini Z (2018) Nat Prod Res 33:1617–1623
4. Lown JW, Joshua AV, Lee JS (1982) Biochemistry 21:419–428
5. Ahrén B (2009) Best Pract Res Clin Endocrinol Metab 23:487–498
6. Krishnamurthy R, Snieckus V (2017) Synlett 28:27–29
7. Corey EJ, Gin DY, Kania RS (1996) J Am Chem Soc 118:9202–9203
8. Benner SA, Kim HJ, Kim MJ, Ricardo A (2010) Cold Spring Harb Perspect Biol 2:a003467
9. Kouznetsov VV, Hernández JG (2022) RSC Adv 12:20807–20828
10. Eslami M, Dekamin MG, Motlagh L, Maleki A (2018) Green Chem Lett Rev 11:36–46
11. Yaghoobi M, Zareyee D, Khalilzadeh MA (2022). Inorg Nano-Met Chem. https://doi.org/10.1080/24701556.2022.2081194
12. Zareyee D, Rad AS, Ataei Z, Javadi SH, Khalilzadeh MA (2018) Appl Organomet Chem 32:e4422
13. Reinares-Fisac D, Aguirre-Díaz LM, Iglesias M, Snejko N, Gutiérrez-Puebla E, Monge MÁ, Gándara F (2016) J Am Chem Soc 138:9089–9092
14. Sun M, Liu W, Wu W, Li Q, Song D, Yan L, Mohammadnia M (2021). Inorg Nano-Met Chem. https://doi.org/10.1080/24701556.2021.1977819
15. Tejwan N, Saini AK, Sharma A, Singh TA, Kumar N, Das J (2021) J Controlled Release 330:132–150
16. Bharat TC, Mondal S, Gupta HS, Singh PK, Das AK (2019) Mater Today Proc 11:767–775
17. Kaur M, Sharma C, Sharma N, Jamwal B, Paul S (2020) ACS Appl Nano Mater 3:10310–10325
18. Yang X, He J, Yang Q, Jiao R, Liao G, Wang D (2019) J Colloid Interface Sci 551:16–25
19. Aghazadeh M, Karimzadeh I, Ganjali MR, Behzad A (2017) J Mater Sci Mater Electron 28:18121–18129
20. Aghazadeh M, Karimzadeh I, Ganjali MR (2018) Mater Lett 228:137–140
21. Rezazadeh Z, Soleimani F, Mahmoudi B, Nasseri MA, Kazemnejadi M (2021) Appl Phys A 127:1–13
22. Ibrahim EMM, Abdel-Rahman LH, Abu-Dief AM, Elshafaie A, Hamdan SK, Ahmed AM (2018) Mater Res Bull 99:103–108
23. Li F, Zhen H, Li L, Li Y, Wang Q, Cheng X (2022) Mater Today Energy 26:100999
24. Malgras V, Ji Q, Kamachi Y, Mori T, Shieh FK, Wu KCW, Ariga K, Yamauchi Y (2015) Bull Chem Soc Jpn 88:1171–1200
25. Salehizadeh H, Hekmatian E, Sadeghi M, Kennedy K (2012) J Nanobiotechnol 10:1–7
26. Gadgeel AA, Mhaske ST, Duerr C, Liu KL (2019) J Inorg Organomet Polym Mater 29:1688–1700
27. Salihov SV, Ivanenkov YA, Krechetov SP, Veselov MS, Sviridenkova NV, Savchenko AG, Klyachko NL, Golovin YI, Chufarova NV, Beloglazkina EK, Majouga AG (2015) J Magn Magn Mater 394:173–178
28. Zhang W, Shen F, Hong R (2011) Particuology 9:179–186
29. Kazemnejadi M, Nasseri MA, Sheikh S, Rezazadeh Z, Gol SAA (2021) RSC Adv 11:15989–16003
30. Lagunas A, IPayeras AM, Jimeno C, Pericàs MA (2006). Chem Commun. https://doi.org/10.1039/b517812f
31. Hu Y, Ren M, Kazemnejadi M (2021) Chem Open 10:775–783
32. Zhu Y, Xu G, Kazemnejadi M (2021) New J Chem 45:11662–11671
33. Jasim SA, Tanjung FA, Sharma S, Mahmoud MZ, Kadhim SB, Kazemnejadi M (2022) Res Chem Intermed 48:3547–3566
34. Jasim SA, Abdulkadhim AH, Yasin G, Abdelbasset WK, Jawad MA, Kazemnejadi M (2022). J Saudi Chem Soc. https://doi.org/10.1016/j.jscs.2022.101487
35. Bellamy FD, Ou K (1984) Tetrahedron Lett 25:839–842
36. Shoaeifar P, Abbasian M, Entezami AA (2007) J Polym Res 14:45–52
37. Lakhera SK, Venkataramana R, Watts A, Anpo M, Neppolian B (2017) Res Chem Intermed 43:5091–5102
38. Mahmoudi B, Rostami A, Kazemnejadi M, Hamah-Ameen BA (2020) Green Chem 22:6600–6613
39. Kazemnejadi M, Alavi SA, Rezazadeh Z, Nasseri MA, Allahresani A, Esmaeilpour M (2019) J Mol Struct 1186:230–249
40. Maghfirah A, Ilmi MM, Fajar ATN, Kadja GTM (2020) Mater Today Chem 17:100348
41. Zhang X, Chen Z, Liu X, Hanna SL, Wang X, Taheri-Ledari R, Maleki A, Li P, Farha OK (2020) Chem Soc Rev 49:7406–7427
42. Bo X, Zhang Q, Li X, Zhao Y (2020) J Sol-Gel Sci Technol 93:324–331
43. Yakin FE, Barisik M, Sen T (2020) J Phys Chem C 124:19579–19587
44. Yang J, Fan L, Xu Y, Xia J (2017). J Nanopart Res. https://doi.org/10.1021/acs.jpcc.0c04602
45. Sardarian AR, Kazemnejadi M, Esmaeilpour M (2021) Appl Organomet Chem 35:e6051

46. Kasote DM, Lee JH, Jayaprakasha GK, Patil BS (2021) Nanomaterials 11:1016
47. Xu W, Yuan L, Liang G, Gu A (2022) Polym Adv Technol 33:1642–1654
48. Bakhtiarzadeh Z, Rouhani S, Karimi Z, Rostamnia S, Msagati TA, Kim D, Jang HW, Ramakrishna S, Varma RS, Shokouhimehr M (2021) Mol Catal 509:111603
49. Nasseri MA, Rezazadeh Z, Kazemnejadi M, Allahresani A (2020) Dalton Trans 49:10645–10660
50. Zarnegaryan A, Beni AS (2021) J Organomet Chem 953:122043
51. Yang C, Fontaine O, Tarascon JM, Grimaud A (2017) Angew Chem 129:8778–8782
52. Pääkkönen T, Bertinetto C, Pönni R, Tummala GK, Nuopponen M, Vuorinen T (2015) Appl Catal A Gen 505:532–538
53. Eltayeb NE (2020) Indones J Chem 20:451–457
54. Venkataramanan NS, Kuppuraj G, Rajagopal S (2005) Coord Chem Rev 249:1249–1268
55. Chen Z, Zheng Y, Liu Y, Zhang W, Wang Y, Guo X, Tang X, Zhang Y, Wang Z, Zhang T (2019) Mater Chem Phys 238:121893
56. Sharma S, Chauhan P, Husain S (2021) Adv Mater Proc 1:220–225
57. Kazemnejadi M, Nikookar M, Mohammadi M, Shakeri A, Esmaeilpour M (2018) J Colloid Interface Sci 527:298–314
58. Chen SH, Zhu JJ, Li PH, Sun YF, Yang M, Huang XJ (2022) Chem Eng J 430:132959
59. Wang Z, Lai C, Qin L, Fu Y, He J, Huang D, Li B, Zhang M, Liu S, Li L, Zhang W (2020) Chem Eng J 392:124851
60. Nasseri MA, Ramezani-Moghadam S, Kazemnejadi M, Allahresani A (2020) Res Chem Intermed 46:4233–4256
61. Rangraz Y, Heravi MM, Elhampour A (2021) Chem Rec 21:1985–2073
62. Nasseri MA, Alavi SA, Kazemnejadi M, Allahresani A (2019) ChemistrySelect 4:8493–8499
63. Verma K, Sharma A, Badru R (2021) Curr Res Green Sustain Chem 4:100060
64. Zhao J, Hernández WY, Zhou W, Yang Y, Vovk EI, Capron M, Ordomsky V (2020) ChemCatChem 12:238–247
65. Ishida T, Taketoshi A, Haruta M (2020) Gold nanoparticles for oxidation reactions: critical role of supports and au particle size. In: Kobayashi S (ed) Nanoparticles in catalysis. Topics in organometallic chemistry, vol 66. Springer, Cham

Authors and Affiliations

Eman Khalaf[1] · Ameer A. Alameri[2] · Jitendra Malviya[3] · T. CH. Anil Kumar[4] · Farag M. A. Altalbawy[5,6] · Raed H. C. Alfilh[7] · Milad Kazemnejadi[8]

✉ Milad Kazemnejadi
miladkazemnejad@yahoo.com

1 Pharmacy Department, Al-Maarif University College, Ramadi, Iraq

2 Chemistry Department, University of Babylon, Babylon, Iraq

3 Department of Life Sciences and Biological Sciences, IES University, Bhopal, Ratibad, Madhya Pradesh, India

4 Department of Mechanical Engineering, Vignan's Foundation for Science Technology and Research, Vadlamudi, India

5 Department of Chemistry, University College of Duba, University of Tabuk, Tabuk 12613, Saudi Arabia

6 National Institute of Laser Enhanced Sciences (NILES), University of Cairo, Giza 12613, Egypt

7 Refrigeration & Air-Conditioning Technical Engineering Department, College of Technical Engineering, The Islamic University, Najaf, Iraq

8 Department of Chemistry, Faculty of Science, Golestan University, Gorgān, Iran